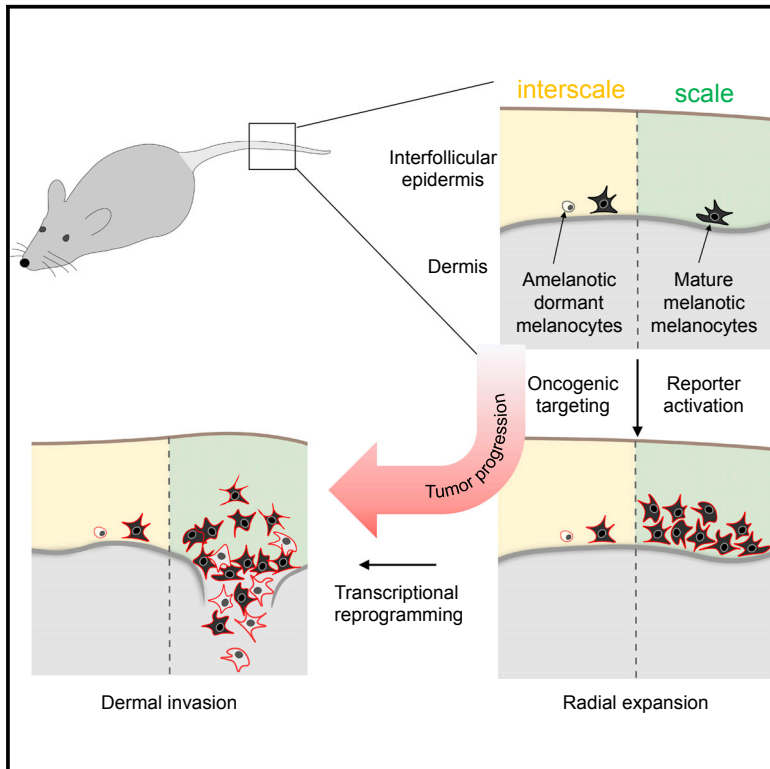


Mouse Cutaneous Melanoma Induced by Mutant BRAF Arises from Expansion and Dedifferentiation of Mature Pigmented Melanocytes

Graphical Abstract



Authors

Corinna Köhler, David Nittner, Florian Rambow, ..., Holger Gerhardt, Cedric Blanpain, Jean-Christophe Marine

Correspondence

jeanchristophe.marine@vib.kuleuven.be

In Brief

The precise cellular origin of cutaneous melanoma has been a topic of intense debate. Using a refined mouse model that faithfully recapitulates key histopathological features of early stages of human melanomagenesis, Köhler et al. report that melanoma can arise from mature, pigment-producing melanocytes located within the interfollicular epidermis.

Highlights

- Melanoma induced in mouse tail epidermis recapitulates human disease features
- Amelanotic melanocytes reside within niches that suppress melanoma formation
- Mature, pigment-producing interfollicular melanocytes efficiently form tumors
- Melanoma formation involves transcriptional reprogramming and dedifferentiation



Mouse Cutaneous Melanoma Induced by Mutant BRAf Arises from Expansion and Dedifferentiation of Mature Pigmented Melanocytes

Corinna Köhler,^{1,2,10} David Nittner,^{1,2,10} Florian Rambow,^{1,2} Enrico Radaelli,^{3,4} Fabio Stanchi,⁵ Niels Vandamme,⁶ Arianna Baggiolini,⁷ Lukas Sommer,⁷ Geert Berx,⁶ Joost J. van den Oord,⁸ Holger Gerhardt,⁵ Cedric Blanpain,⁹ and Jean-Christophe Marine^{1,2,11,*}

¹Laboratory for Molecular Cancer Biology, VIB Center for Cancer Biology, VIB, 3000 Leuven, Belgium

²Laboratory for Molecular Cancer Biology, Department of Oncology, KULeuven, 3000 Leuven, Belgium

³Mouse Histopathology Core Facility, VIB Center for Brain Disease, VIB, 3000 Leuven, Belgium

⁴Comparative Pathology Core, Department of Pathobiology, School of Veterinary Medicine, University of Pennsylvania, Philadelphia, PA 19104-6051, USA

⁵Vascular Patterning Laboratory, VIB Center for Cancer Biology, VIB, 3000 Leuven, Belgium

⁶Molecular and Cellular Oncology Laboratory, Cancer Research Institute Ghent (CRIG), 9052 Ghent University, Ghent, Belgium

⁷Stem Cell Biology, Institute of Anatomy, University of Zurich, 8057 Zurich, Switzerland

⁸Laboratory of Translational Cell and Tissue Research, Department of Pathology, KULeuven and UZ Leuven, 3000 Leuven, Belgium

⁹Laboratory of Stem Cells and Cancer, Welbio, Université Libre de Bruxelles, 1070 Bruxelles, Belgium

¹⁰These authors contributed equally

¹¹Lead Contact

*Correspondence: jeanchristophe.marine@vib.kuleuven.be

<https://doi.org/10.1016/j.stem.2017.08.003>

SUMMARY

To identify the cells at the origin of melanoma, we combined single-cell lineage-tracing and transcriptomics approaches with time-lapse imaging. A mouse model that recapitulates key histopathological features of human melanomagenesis was created by inducing a BRAfV600E-driven melanomagenic program in tail interfollicular melanocytes. Most targeted mature, melanin-producing melanocytes expanded clonally within the epidermis before losing their differentiated features through transcriptional reprogramming and eventually invading the dermis. Tumors did not form within interscales, which contain both mature and dormant amelanotic melanocytes. The hair follicle bulge, which contains melanocyte stem cells, was also refractory to melanomagenesis. These studies identify varying tumor susceptibilities within the melanocytic lineage, highlighting pigment-producing cells as the melanoma cell of origin, and indicate that regional variation in tumor predisposition is dictated by microenvironmental cues rather than intrinsic differences in cellular origin. Critically, this work provides *in vivo* evidence that differentiated somatic cells can be reprogrammed into cancer initiating cells.

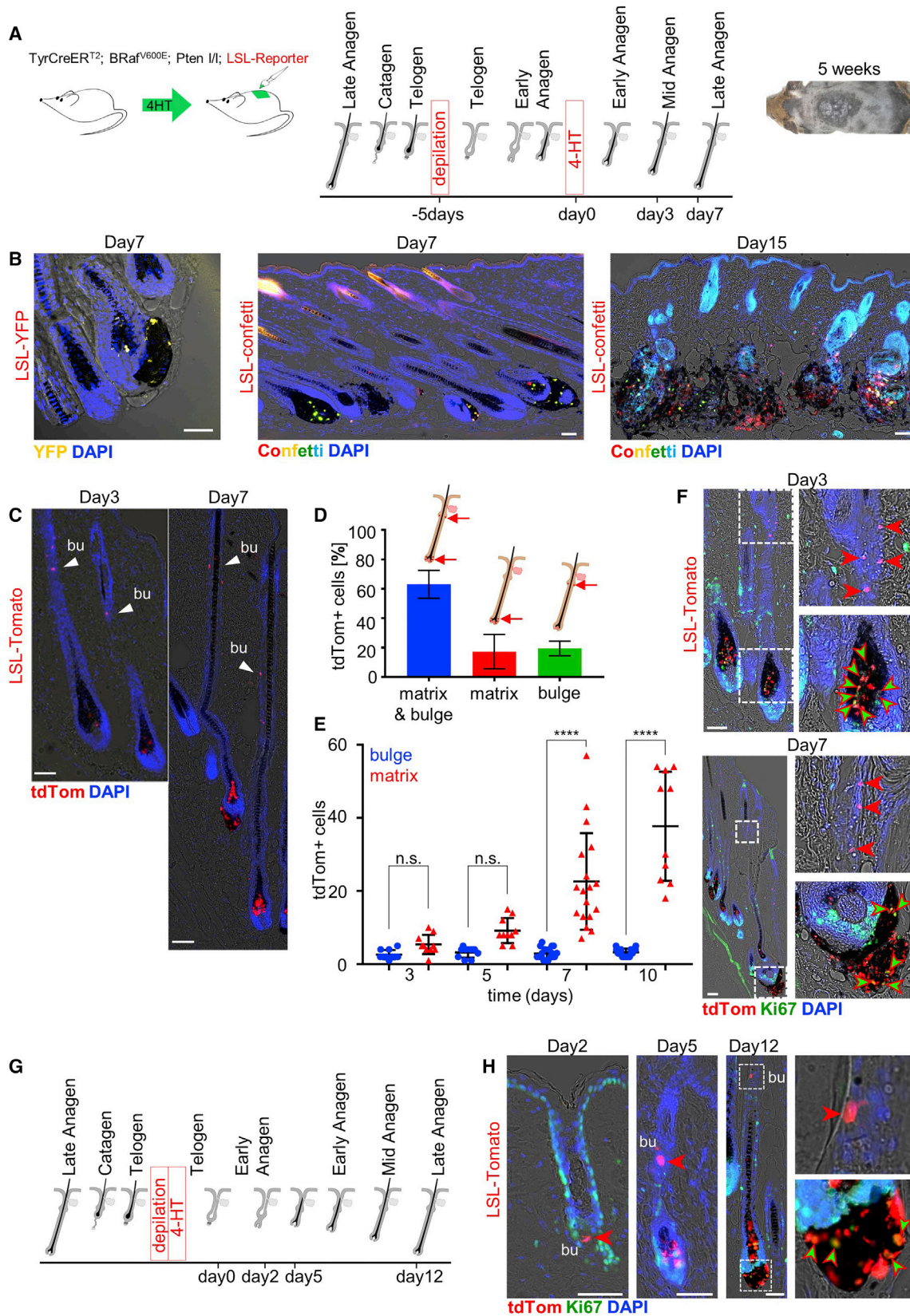
INTRODUCTION

Identification of the cancer cell of origin is a critical step toward earlier detection of malignancies, better prediction of tumor

behavior, and development of preventive therapies. Cutaneous melanoma is the leading cause of death from diseases of the skin. One way to reduce the morbidity and mortality from cutaneous melanoma is diagnosis at an early stage when the prognosis for cure by surgical removal is excellent. There is indeed much evidence that thin melanomas have a favorable prognosis (Balch et al., 2001). Identifying and characterizing the melanoma cell-of-origin will not only help identifying markers for early detection but also elucidate the molecular mechanisms underlying melanoma plasticity and intra-tumor heterogeneity, which, in turn, should help understand tumor cell responses to clinical treatments, drug resistance, tumor relapse, and metastatic spread.

All melanocytic neoplasms, ranging from benign lesions (or nevi) to malignant melanomas, originate from the neural-crest-derived melanocytic lineage. During embryonic development, melanoblasts, the precursors of differentiated melanocytes, colonize the skin and few other tissues throughout the body (Mort et al., 2015). In human skin, the vast majority of melanocytes reside at the dermo-epidermal junction, where their main function is to provide melanin pigment to their neighboring keratinocytes. Similarly, the murine tail contains interfollicular (IF) melanocytes and a pigmented IF epidermis. Both mouse and human melanocytes also colonize hair follicles (HFs), where they contribute melanin to the hair shaft (Mort et al., 2015).

The HF undergoes cyclic expansion (anagen) and regression (catagen) in response to normal growth or as a stress response following hair removal. During the catagen phase, virtually all differentiated, pigmented melanocytes are eliminated by apoptosis. During the anagen phase, there is expansion of the melanocyte pool from the non-pigment-producing melanocyte stem cells (MSCs) that are located in the hair bulge and differentiation of the transient amplifying cells into melanin-producing melanocytes, which repopulate the lower HF or matrix. HF



(legend on next page)

MSCs can be stimulated by wound healing or ultraviolet radiation to migrate to the IF epidermis and differentiate into pigment-producing melanocytes (Chou et al., 2013; Nishimura, 2011; Nishimura et al., 2002).

Recent evidence demonstrated that HFs are not the only source of IF melanocytes (Glover et al., 2015). Mouse tail skin lacking appendages does maintain a stable number of melanocytes, including a low frequency (1.5% of the total melanocyte population) of amelanotic melanocytes, into adult life (Glover et al., 2015). It has been proposed that these amelanotic melanocytes may serve as a reservoir used for repopulation upon large scale melanocyte loss and therefore function as IF MSCs (Glover et al., 2015). Whether, just like in the HF bulge, IF melanocyte and keratinocyte stem cells share a common niche is unknown. Importantly, recognition of these distinct melanocyte cell populations and their potential for different behaviors also raises major questions about their respective roles in melanomagenesis. In particular, whether (hair follicle bulge and IF) melanocyte stem cells and/or mature pigment-producing melanocytes are equally competent for tumorigenesis is unknown (Boiko et al., 2010; Hoerter et al., 2012; Kaufman et al., 2016).

Here, we used mouse genetics, lineage-tracing approaches, time-lapse imaging, and single-cell profiling techniques to identify the cell of origin of *BRAF*^{V600E}-induced melanoma and study the temporal morphological and molecular changes that occur in tumor-initiating cells from the first oncogenic hit to the development of invasive melanoma. Our studies identify varying tumor susceptibilities among the different melanocytic lineage subpopulations in the mouse skin, unexpectedly highlighting mature pigment-producing cells as “hot spots” for tumor initiation.

RESULTS

The HF Bulge Stem Cell Niche Is Refractory to *BRAF*^{V600E}-Induced Melanomagenesis

HFs are well-recognized reservoirs of both MSCs and their differentiated progeny. To determine whether HF MSCs and their progeny are similarly competent to induce melanoma formation, we expressed *BRaf*^{V600E}, the most prevalent mutation in human melanoma, in both melanocytic compartments. We used mice expressing a 4-hydroxytamoxifen (4-HT)-inducible form of Cre under the control of the melanocyte-specific tyrosinase promoter, designated *Tyr::CreER*^{T2/+} (Bosenberg et al., 2006). This particular allele was chosen because its ability to drive Cre-dependent recombination in both bulge MSCs and all of their

progeny upon topical application of 4-HT to dorsal skin had previously been suggested based on long-term lineage-tracing experiments (Bosenberg et al., 2006; Harris and Pavan, 2013). Accordingly, genetic ablation of *Sox10* in adult mice using this particular allele led to a permanent reduction in the number of MSCs and an inability of remaining MSCs to fully replenish the bulb melanocyte population in newly generated hairs, thus unambiguously demonstrating efficient Cre-mediated locus recombination in the MSC compartment (Harris et al., 2013). The *Tyr::CreER*^{T2/+} mice were crossed to mice carrying a conditional *BRaf*^{V600E} allele (*BRaf*^{CA/+}), which expresses *BRaf*^{V600E} only after 4-HT administration (Dankort et al., 2007). Because loss-of-function of *Pten*, an event commonly seen in *BRAF*^{V600E} mutant human melanomas, is required to initiate full-blown melanomagenesis (Damsky et al., 2011) we created *Tyr::CreER*^{T2/+}; *BRaf*^{CA/+}; *Pten*^{l/l} mice (Figure S1). In order to fate map the cells that undergo Cre-mediated recombination, we crossed these compound mice with mice carrying two different inducible ROSA26R promoter-driven reporter alleles, the YFP (Srinivas et al., 2001) and tdTomato (Madisen et al., 2010), and generated *Tyr::CreER*^{T2/+}; *BRaf*^{CA/+}; *Pten*^{l/l}; ROSA26R^{L^{SL}-YFP/+} (hereafter BRaf/Pten/YFP) and *Tyr::CreER*^{T2/+}; *BRaf*^{CA/+}; *Pten*^{l/l}; ROSA26R^{L^{SL}-tdTomato/+} (hereafter BRaf/Pten/tomato) mice (Figure S1). We also crossed *Tyr::CreER*^{T2/+}; *BRaf*^{CA/+}; *Pten*^{l/l} mice to mice carrying the Br2.1 (also called Confetti) allele under the control of the same ROSA26R promoter (Di Girolamo et al., 2015) (Figure S1). This reporter allele allows the random, inducible, and tissue-specific expression of one of four distinct fluorescent proteins (green/GFP, yellow/YFP, red/RFP, cyan/CFP) in each targeted cell. To increase the number of possible color combinations to 10 (Di Girolamo et al., 2015), we generated homozygous Confetti mice (*Tyr::CreER*^{T2/+}; *BRaf*^{CA/+}; *Pten*^{l/l}; ROSA26R^{L^{SL}-Confetti/L^{SL}-Confetti} hereafter BRaf/Pten/Confetti) expressing 2 color tags per cell.

Five days after depilation, the dorsal skin of adult BRaf/Pten/Reporter mice was treated with 4-HT (Figure 1A). At this time point, HFs contain both bulge amelanotic melanocytes and their progeny, including melanin-producing melanocytes in the lower HF region or matrix (Müller-Röver et al., 2001). As expected, macroscopic melanoma lesions appeared within 5 weeks post-4-HT exposure (Damsky et al., 2011) (Figure 1A). Prior to this, at 7 days post-4-HT exposure, reporter gene expression was only detected in HFs (Figure 1B). Clonal expansion was clearly visible in multiple HFs and appeared confined to the lower HF region, eventually leading to the rupture of HFs and dissemination of melanoma cells into the dermis (Figure 1B). Experiments

Figure 1. *BRaf*^{V600E}-Induced Melanomagenesis on the Back Skin of Adult Mice

- (A) Treatment scheme used to activate the melanomagenic program on the back skin of BRaf/Pten/reporter mice.
 (B) Endogenous reporter expression in hair matrices of the back skin 7 and 15 days after topical application of 4-HT.
 (C) Endogenous tdTomato expression in HFs 3 and 7 days after topical application of 4-HT.
 (D) Quantification of targeting efficiency of both HF melanocyte cell compartments (n = 40 HFs; 3 mice). The bar diagram represents the relative target frequencies (as percentage), error bars represent SD.
 (E) Quantification of cell number (n = 30 HFs; 3 mice) of tdTomato expressing cells in the hair bulge and lower hair matrix area. The dotplot represents individual counts and mean, error bars represent SD. ****p < 0.0001; n.s., not significant, one-way ANOVA.
 (F) Immunostaining for Ki67 and endogenous tdTomato expression in back skin HFs 3 and 7 days after topical application of 4-HT.
 (G) Treatment scheme used to activate the melanomagenic program in activated bulge melanocytes.
 (H) Immunostaining for Ki67 and endogenous tdTomato expression in back skin HFs 2, 5, and 12 days after topical application of 4-HT. DAPI nuclear staining is depicted in blue.
 Scale bars, 50 μm. bu, bulge.

performed with BRaf/Pten/Confetti mice demonstrated the multiclonal nature of these lesions (Figure 1B).

A detailed kinetic analysis was performed on BRaf/Pten/*tdTomato* mouse background. As described above, the *Tyr::CreER^{T2/+}* allele was previously shown to drive recombination in both bulge MSCs and all of their progeny (Bosenberg et al., 2006). However, because the efficiency of the CreER recombinase varies substantially with different combinations of CreER source and loxP target (i.e., reporter allele chosen), the genetic background of the mice and the level and timing of 4-HT exposure, we carefully quantified the activity of the Cre-driver in the entire melanocytic lineage on the BRaf/Pten/*tdTomato* background. Importantly, shortly after CreER induction, the frequency of *tdTomato*-positive cells in the upper (bulge) and lower (matrix) HF melanocytic compartments was comparable (Figures 1C and 1D). A PCR-based approach further demonstrated that Cre-mediated recombination at both the *BRaf^{CA}* and *Pten* loci was as efficient in the bulge compartment as in the entire melanocytic lineage (Figures S2B and S2C). Consistent with a high efficiency of targeting at both loci, expression of phosphorylated Erk (P-Erk) and Akt (P-Akt) was systematically detected in the bulge compartment of BRaf/Pten/*tdTomato*, but not wild-type, mice 3–5 days following 4-HT exposure (Figure S2D). Unexpectedly, and despite the above-described evidence of activation of MAPK and PI3K signaling, the number of reporter-positive cells remains constant in the bulge region over the course of the experiment (Figure 1E). In contrast, clonal expansion was observed from day 5 onward in the lower HF region (Figure 1E), a compartment that only contains differentiated, melanin-pigment-producing cells. Accordingly, expression of Ki67, a marker of cell proliferation, was only detected in the lower HF, but not in the bulge (Figure 1F). These data indicated that melanocytes located in the bulge are resistant to *BRaf^{600E}*-induced melanoma formation.

To further substantiate this finding, we activated the melanogenic program specifically in the bulge compartment by treating the animals with 4-HT at P20, when HFs are in the first telogen phase and thought to contain exclusively quiescent bulge MSCs (Müller-Röver et al., 2001). Although reporter-positive cells were readily detectable in the bulge compartment 2 days following 4-HT treatment, there was no evidence of expansion of the targeted cells (none of the 30 *tdTomato*-positive HFs exhibited more than 3 *tdTomato*-positive cells in the bulge; $n = 3$ mice) up to 13 days following induction (Figure S3).

Depilation removes the hair shafts, which contain all pigmented matrix melanocytes, and thereby synchronizes the HF in the telogen phase (Müller-Röver et al., 2001). This procedure also stimulates telogen HFs to enter anagen by removing an inner bulge layer of cells that maintain immature melanocyte stem cells, located in the outer bulge layer, in a quiescent state (Hsu et al., 2011). We therefore sought to target specifically activated bulge melanocytes by exposing BRaf/Pten/*tdTomato* mice (age 49 days) to 4-HT immediately after depilation (Figure 1G). 54% of telogen HFs contained *tdTomato*-positive cells within their bulge (27 out of 50 HFs; $n = 3$) 2 days post-4-HT exposure. There was no evidence of proliferation nor of clonal expansion of cells within the bulge (0 out of 50; $n = 3$) up to 12 days post-treatment. In contrast, clonal expansion and evidence of cell proliferation were seen in 84% (42 out of 50; $n = 3$) of HFs containing *tdTo-*

mat-positive cells within their bulge, but only in the lower HF region and 5 (and 12) days post-treatment (Figure 1H). These data are consistent with the HF bulge microenvironment being refractory to *BRaf^{600E}*-driven tumor initiation and indicate that melanoma lesions can originate from bulge melanocytes but only after these cells have migrated out of the bulge niche and reached the lower HF region as mature melanogenic melanocytes.

Tumors Originating from Mouse Tail IF Melanocytes Recapitulate the Bi-Phasic Growth Pattern Characteristic of Human Melanoma In Situ

Because *BRaf/Pten* back-skin melanomas lack epidermal involvement (Figure S4), and HF involvement is seen only rarely in human melanoma, the clinical relevance of the above-described model of melanoma remains limited. Because the vast majority of human melanoma arises from melanoma in situ, an early stage of melanomagenesis in which transforming melanocytes proliferate in an irregular pattern entirely within the interfollicular-epidermis (IFE), it has been postulated that the cell of origin of most human melanomas may reside in the IFE (Shain and Bastian, 2016). Similarly to human skin, and unlike dorsal skin, mouse tail skin contains interfollicular melanocytes. We therefore sought to induce the *BRaf^{600E}*-dependent melanogenic program in tail IF melanocytes. Lineage tracing experiments in BRaf/Pten/YFP mice demonstrated that the topical application of a low dose of 4-HT on the mouse tail permits targeting of the IF melanocytic compartment at clonal density and eventually the development of tail melanomas (Figures 2A–2C). Interfollicular BRaf/Pten/YFP mutant cells expanded radially in the epidermis to form lesions that resembled human in situ melanomas (Figure 2D). In this radial growth phase (RGP), primary melanoma cells, which still rely on growth factors produced by the surrounding keratinocytes, proliferate above the epidermal basement membrane and are strictly confined to the epidermis. At later time points (1.5–2 months post-4-HT), multifocal dermal invasions of atypical melanoma cells became apparent. This is reminiscent of the human invasive RGP (iRGP) melanomas, a stage in which individual or small clusters of melanoma cells invade shallowly into the superficial reticular dermis and have little or no initial capacity for proliferation (Figure 2D). After 2–2.5 months, dermally invasive and S100-positive melanomas were observed that resembled human vertical growth phase (VGP) lesions (Figure 2D). VGP defines tumors that acquire proliferative capacity and grow vertically, filling the papillary dermis. Thus, the application of low dose 4-HT to the tails of *Tyr::CreER^{T2/+}; BRaf^{CA/+}; Pten^{fl}* mice initiates a sequence of events that recapitulate the characteristic bi-phasic growth pattern and key histological features observed during development of the most common histogenetic subtypes of human melanoma (Clark et al., 1975).

Amelanotic and Melanogenic IF Melanocytes Exhibit Distinct Spatial Distribution and Proliferative Behaviors

Mouse tail IFE contains both mature, pigment-producing melanocytes and a low frequency of amelanotic melanocytes, which may serve as reservoirs of interfollicular MSCs (Glover et al., 2015). To assess whether the amelanotic tail compartment is efficiently targeted by the *Tyr::CreER^{T2}* allele, we performed lineage tracing at homeostasis by generating *Tyr::CreER^{T2/+};*

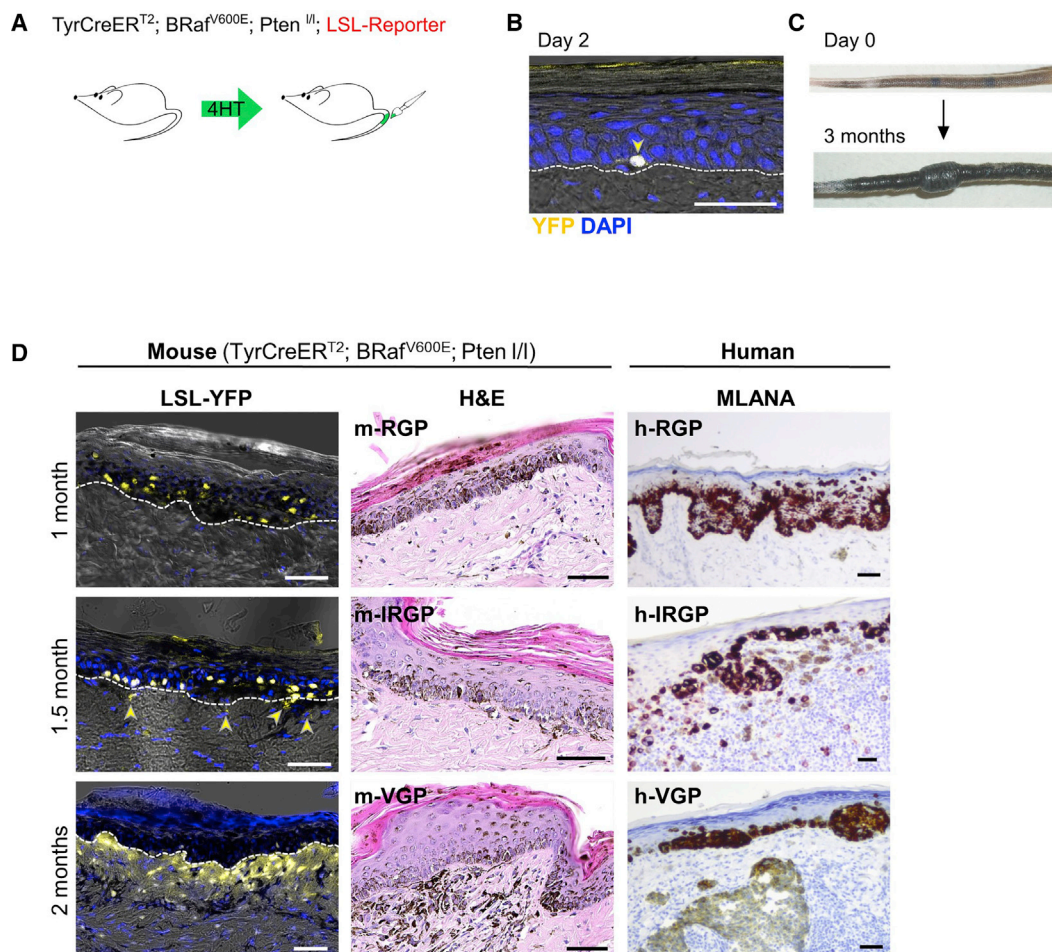


Figure 2. Mimicking the Development of Human Melanoma In Situ in Mice

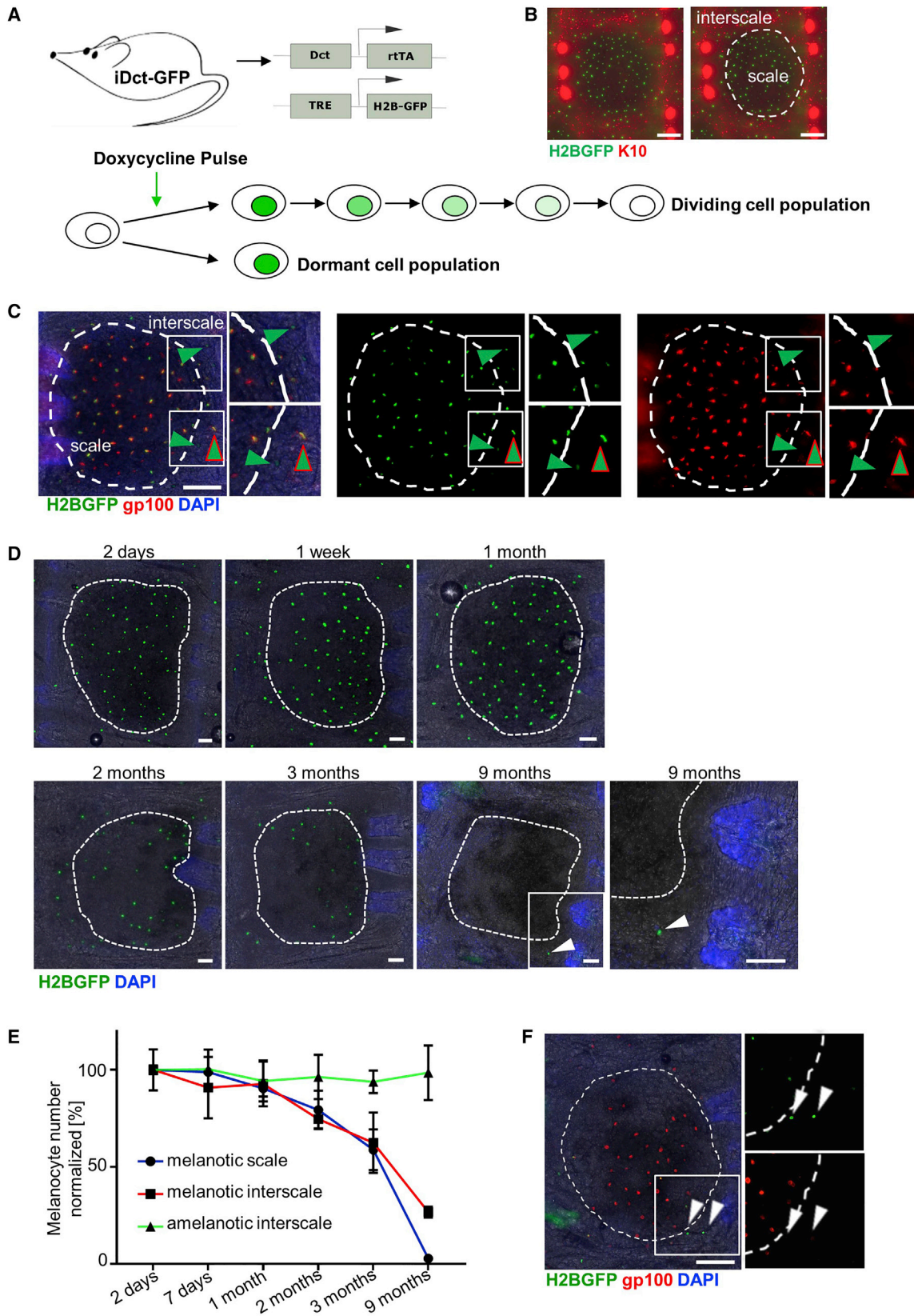
(A) Treatment scheme used to activate the *BRaf*^{V600E}-driven melanomagenic program in IF melanocytes. (B) Endogenous YFP expression in a targeted interfollicular melanocyte 2 days after topical application of 4-HT. (C) Area of treatment on the tail skin and macroscopic melanoma lesion on the tail skin 3 months after topical application of 4-HT. (D) Endogenous reporter (YFP) expression (left) and H&E staining (middle) in *BRaf*/*Pten*/YFP tail skin sections at specified time points after the topical application of 4-HT compared to MLANA (or melan-A) stained human melanoma lesions (right). DAPI nuclear staining is depicted in blue. White and black scale bars, 50 μ m. m-RGP, murine radial growth phase; h-RGP, human radial growth phase; m-IRGP, murine invasive radial growth phase; h-IRGP, human invasive radial growth phase; m-VGP, murine vertical growth phase; h-VGP, human vertical growth phase.

ROSA26R^{LSL-tdTomato/+} mice and painting their tails with 4-HT. We performed immunofluorescence analysis on tail sections using an antibody directed against gp100, a type 1 transmembrane glycoprotein expressed in pigment-producing but not in amelanotic melanocytes. tdTomato/gp100-double positive cells and tdTomato-positive/gp100-negative cells were identified post-4-HT exposure indicating that the *Tyr::CreER*^{T2} allele is capable of driving Cre-mediated recombination in both interfollicular melanocytic subpopulations (Figure S5A).

The tail epidermis is divided into two distinct compartments, scale (K10-negative) and interscale (K10-positive) (Didierjean et al., 1983; Schweizer and Marks, 1977). Whereas few (on average 7.5 cells out of 43.7 per tail unit; 10 units were analyzed; n = 3) tdTomato/gp100-double positive cells were identified in the interscale hinges, the majority (on average 34.9 cells out of 43.7 per tail unit; 10 units were analyzed; n = 3) of these cells are located within the scale regions. In contrast, all tdTomato-posi-

tive tdTomato-positive/gp100-negative amelanotic cells (on average 1.3 cells out of 43.7 per tail unit; 10 units were analyzed, n = 3) were detected in the interscales (Figures S5B and S5C).

To further substantiate this regionalized cell distribution, we used the iDct-GFP mouse model, which allowed doxycycline-inducible expression of H2BGFP in all melanocytic compartments of the HF including MSCs and all their descendants (Zaidi et al., 2011). Importantly, this model permits long-term lineage tracing at single-cell resolution and quantification of the proliferation history in vivo from the amount of H2BGFP fluorescence retained in cells following injection of a single intraperitoneal dose (pulse) of doxycycline (Tumbar et al., 2004; Waghmare et al., 2008) (Figure 3A). Whole-mount tail epidermis demonstrated that H2BGFP-positive cells were detected in both scale (K10-negative) and (K10-positive) interscale compartments (Figure 3B). Importantly, both gp100-positive melanin-producing melanocytes and gp100-negative amelanotic cells could be



(legend on next page)

labeled using this approach (Figure 3C) and, consistent with the tdTomato-lineage tracing experiment, all H2BGFP-positive gp100-negative cells were located in the interscale hinges (Figure 3C). Thus, in contrast to their pigment-producing counterparts, amelanotic melanocytes exclusively localize to interscales.

Long-term pulse chase experiments showed that the intensity of GFP-positivity within scales varied from cell to cell from 2 months post-doxycycline exposure onward, indicating that these cells completed a varying number of cell divisions (Figure 3D). The number of GFP-positive cells within scales gradually decreased over the next few months with only very few positive cells remaining 9 months post-doxycycline exposure (Figures 3D and 3E). This observation indicated that the pigment-producing gp100-positive scale melanocytes are slow dividing cells. In contrast, the number of GFP-positive gp100-negative cells within the interscales (on average 1.1 cells per tail unit, 30 units were analyzed; $n = 3$) remained constant over the entire duration of the experiment (Figures 3E and 3F). Thus, during homeostasis, in contrast to their comparatively more rapidly dividing neighbors, the interscale amelanotic cells represent a quiescent and constant cell population.

Melanoma Efficiently Arises from Mature Pigment-Producing, but Not Amelanotic, IF Melanocytes

We next asked whether these two distinct IF melanocytic subpopulations are both competent to induce melanoma formation. Lineage tracing experiments confirmed that amelanotic (gp100-negative) and melanin-producing melanocytes (gp100-positive) compartments are both targeted on the BRaf/Pten/Reporter backgrounds (Figure 4A and data not shown). Critically, evidence of clonal expansion of reporter-positive cells was only readily detectable within K10-negative scales. In contrast, the number of reporter-positive cells remained constant within the interscale hinges (Figure 4B). Consistently, expression of the proliferation marker Ki67 was only detected in scale, and not in interscale, reporter-positive cells (data not shown).

In keeping with their gp100-immunoreactivity, scale reporter-positive cells exhibited the characteristic dendritic morphology of terminally differentiated melanocytes and did produce high amounts of pigment (Figure 4C). Remarkably, early clonal expansion of reporter- (and Ki67-) positive cells within the scale epidermis was not accompanied by a decrease in gp100-positivity nor in their ability to produce melanin (Figures 4C and 4D).

To further study the cellular dynamics leading to the differential sensitivity to melanoma initiation between melanin-producing and amelanotic melanocytes, we assessed reporter gene

expression at different time points following induction of the Confetti randomizer. A reproducible number of single cell clones emerged both within the scale plates and interscale hinges 1 week post-4-HT (Figures 4E and 4F). Remarkably, 36% (on average 9.1 clones out of 25.3 per tail unit, 10 units were analyzed; $n = 3$) of scale-located targeted cells expanded clonally and the labeled cell fraction (i.e., mean clone size), although relatively broad, increased steadily from 1 week post-induction onward (Figures 4E and 4F). In contrast, there was no evidence of clonal expansion of reporter-positive cells within the interscale hinges (on average 0 clones out of 12.8 per tail unit, 10 units were analyzed; $n = 3$).

Together, these data indicated that pigment-producing, but not amelanotic, melanocytes can efficiently serve as tumor progenitors and that tumor initiation can proceed in the absence of dedifferentiation of oncogene-targeted cells. However, given that our lineage-tracing strategy does not discriminatively label the amelanotic and melanogenic compartments, the possibility that targeted amelanotic melanocytes migrate out of the interscale hinges and serve as tumor initiating cells within scales could not be ruled out. To test this, we performed *in vivo* time-lapse imaging concurrent with lineage tracing of reporter-positive cells (Figure 5A). Tails of BRaf/Pten/tdTomato mice were painted with 4-HT to induce tdTomato expression and imaging begun 5 days after 4-HT exposure and continued for 12 hr (Figure 5B). We analyzed time-lapse videos of 6 consecutive units (scales and interscales) from 3 different mice. Whereas numerous mitotic events were observed during this time period within scales (Figure 5B), none of the interscale tdTomato-labeled cells had divided nor migrated away from their initial position. This experiment clearly demonstrated the ability of oncogene-targeted scale melanocytes to actively and rapidly divide as mature, dendritic melanogenic cells. In order to analyze the proliferative and migratory behaviors of reporter-positive cells for longer periods of time, we also performed time-lapse imaging in which we began to image 3 days post-4-HT exposure and continued to do so every 3 days for a total of 9 days (Figure 5C). Whereas there was no evidence of cell proliferation/division nor of significant cell movement within the interscale hinges, clonal expansion of dendritic melanocytes was observed in all scales (Figure 5C). Thus, the fate of oncogene-targeted melanocytes and their ability to progress to melanoma depends on their location (scale versus interscale) and/or phenotypic characteristics. Whereas mature, dendritic, and pigment-producing cells located within scales were competent to initiate tumor formation, amelanotic melanocytes displayed no detectable tumor-forming capacity within the interscale hinges. Importantly, tumor formation

Figure 3. The Mouse Tail IFE Contains Two Distinct Populations of Melanocytes

- (A) Schematic representation of the experimental strategy used to long-term lineage trace the melanocytic lineage within the tail epidermis of iDct-GFP mice.
 (B) Immunostaining for K10 and endogenous H2BGFP expression on iDct-GFP epidermal whole mount 2 days after intraperitoneal injection of doxycycline.
 (C) Immunostaining for gp100 and endogenous H2BGFP expression on iDct-GFP epidermal whole mount. Arrows highlight the presence—within the interscale hinges—of amelanotic melanocytes (H2BGFP-positive/gp100-negative; green arrows) and melanotic melanocytes (H2BGFP/gp100-double positive; green arrows with red outline).
 (D) Endogenous expression of H2BGFP on epidermal whole mounts at the indicated time points following intraperitoneal injection of doxycycline. Arrows highlight the presence of persisting interscale melanocytes.
 (E) Percentage of cell number over time with respect to cell location and pigmentation status. Error bars represent SD ($n = 3$ mice).
 (F) Immunostaining for gp100 on iDct-GFP epidermal whole mount 9 months after intraperitoneal injection of doxycycline; arrows highlight the presence of quiescent gp100-negative interscale amelanotic melanocytes. Dotted lines mark the scale-interscale junction. DAPI nuclear staining is depicted in blue. Scale bars, 50 μm .

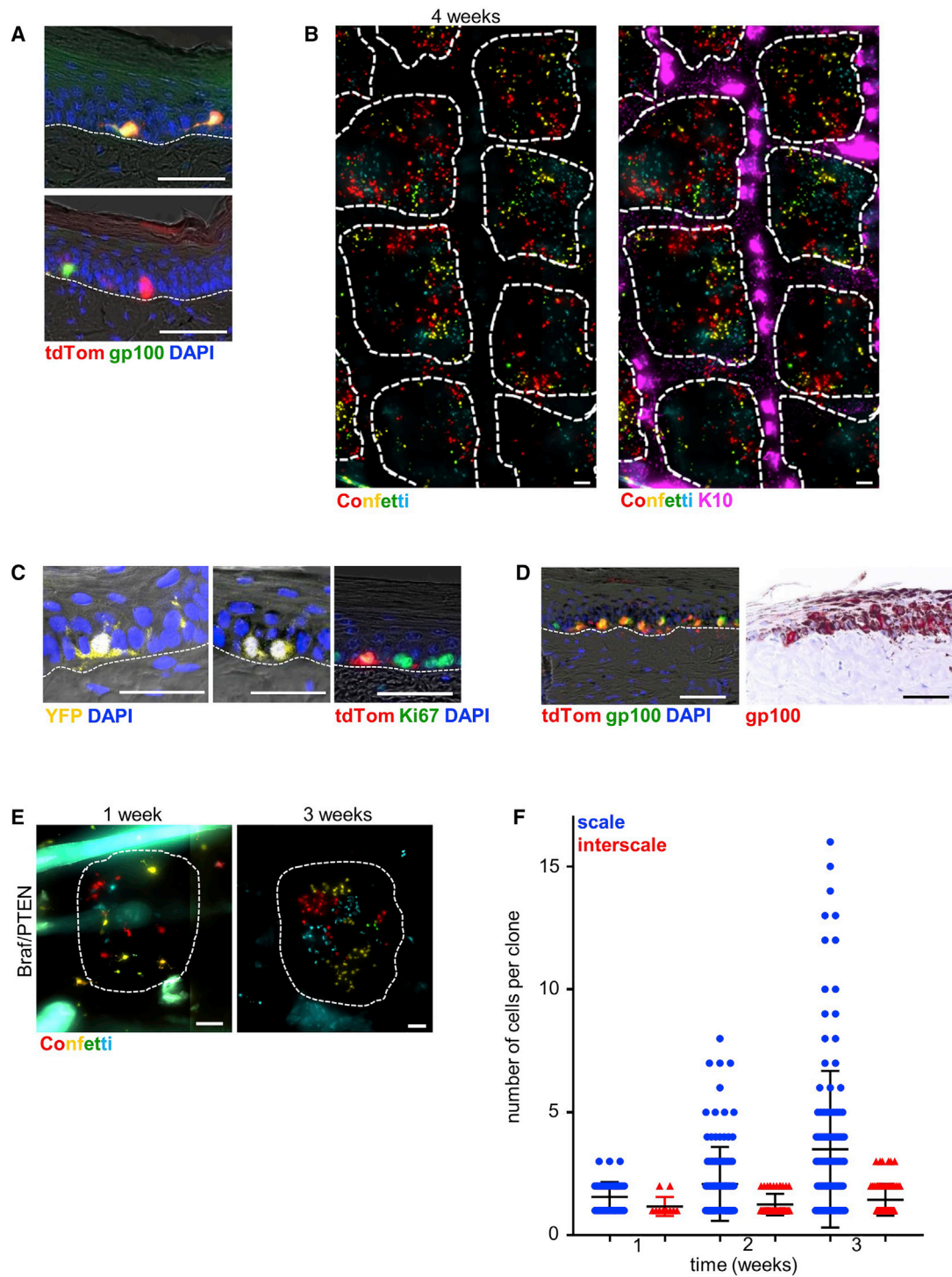


Figure 4. BRAf/Pten Tail Melanoma Originates from Scale Melanocytes

(A) Immunostaining on sections for gp100 and endogenous expression of tdTomato in BRAf/Pten/tomato tail epidermis.

(B) Immunostaining for K10 and endogenous Confetti reporter expression in tail epidermal whole mount of BRAf/Pten/Confetti tail epidermis 4 weeks after topical application of 4-HT.

(C) Endogenous YFP expression on sections in BRAf/Pten/YFP tail skin (left and middle); immunostaining for Ki67 on section and endogenous tdTomato expression (right) in BRAf/Pten/tomato tail skin.

(D) Immunostaining on sections for gp100 and endogenous tdTomato reporter expression in BRAf/Pten/tomato tail skin.

(legend continued on next page)

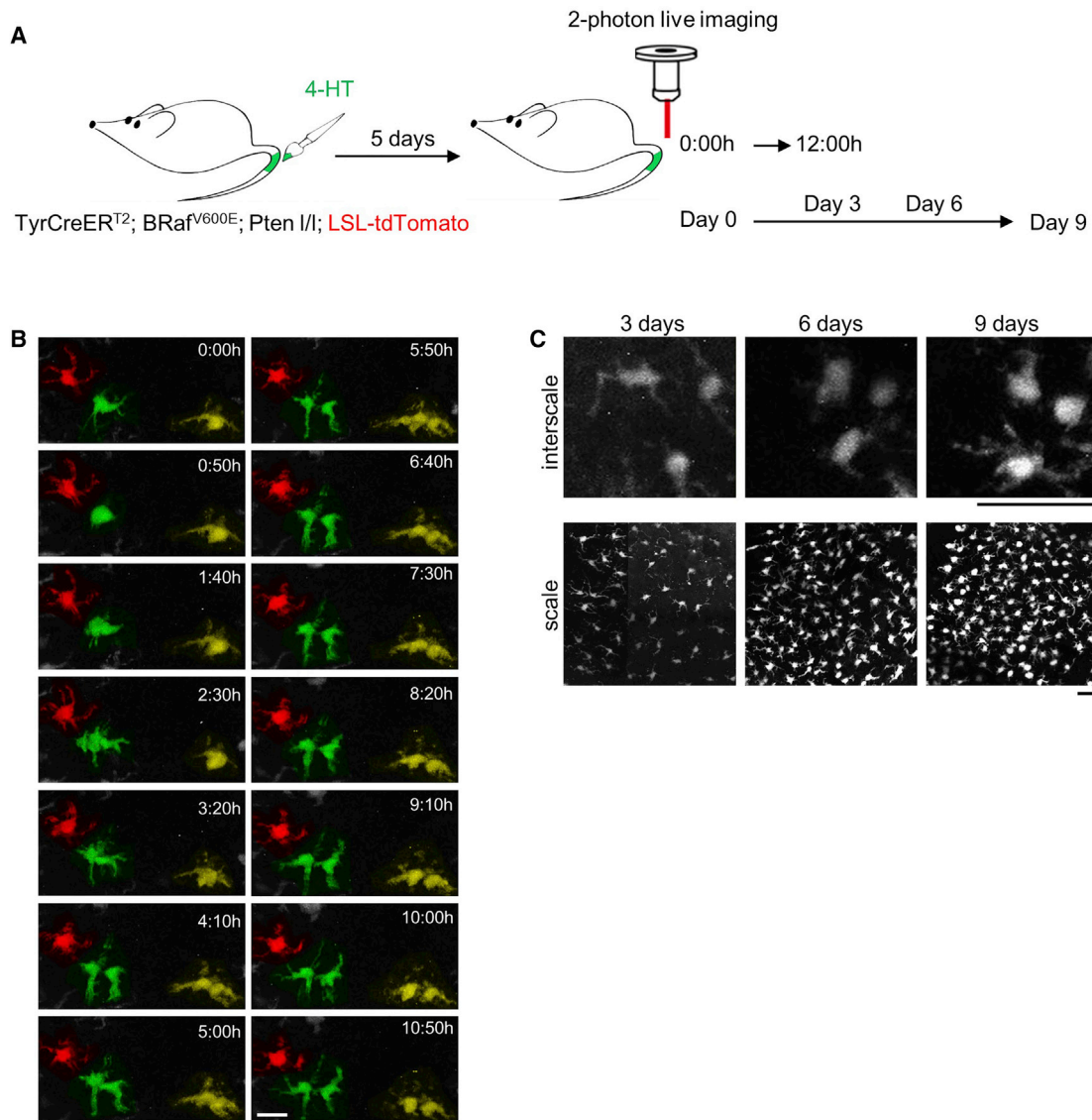


Figure 5. Tracking the Development of Tail Melanoma using Live Imaging

(A) Schematic representation of the experimental strategy used to visualize the development of tdTomato positive melanoma lesions on the tail of living *Braf/Pten/tdTomato* mice.

(B) Stills from a time-lapse movie illustrating dividing tdTomato-positive scale melanocytes 5 days following topical application of 4-HT. Note that cells were artificially color-coded.

(C) Stills from a time-lapse study showing non-dividing tdTomato-positive interscale melanocytes (top) and dividing tdTomato-positive scale melanocytes (bottom) 3, 6, and 9 days after 4HT exposure. Scale bars, 50 μm .

was never observed within interscales despite the presence of a small fraction of pigment-producing gp100-positive melanocytes in this compartment. Together, these data indicated that, similarly to the HF bulge, the interscale microenvironment is not permissive to *BRAF^{V600E}*-driven melanoma formation. Regional variation in tumor predisposition is therefore likely to be dictated by microenvironmental cues rather than intrinsic dif-

ferences in cellular origin (amelanotic versus pigment-producing).

Transcriptome Reprogramming and Loss of Differentiation Markers Precedes Dermal Invasion

Following their intra-epidermal expansion as pigment-producing cells, *BRAF/Pten* tail melanoma cells begin to invade the dermis

(E) Endogenous Confetti reporter expression in *BRAF/Pten/Confetti* tail epidermal whole mounts 1 week and 3 weeks after topical application of 4-HT.

(F) Quantification of cell number per clone of the scale (blue) and interscale (red) region in *BRAF/Pten/Confetti* tail epidermis ($n = 3$ mice per time point). Histograms and error bars represent the mean and SD. Dotted lines mark either the epidermal-dermal or scale-interscale junctions.

DAPI nuclear staining is depicted in blue. Scale bars, 50 μm .

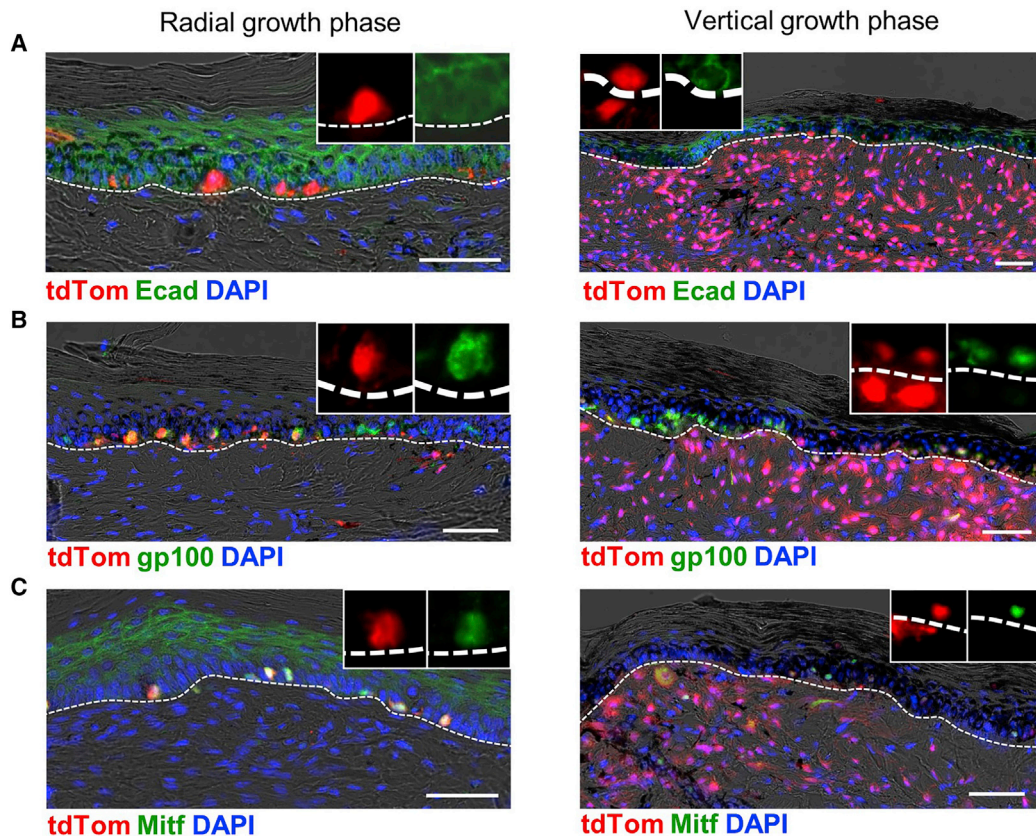


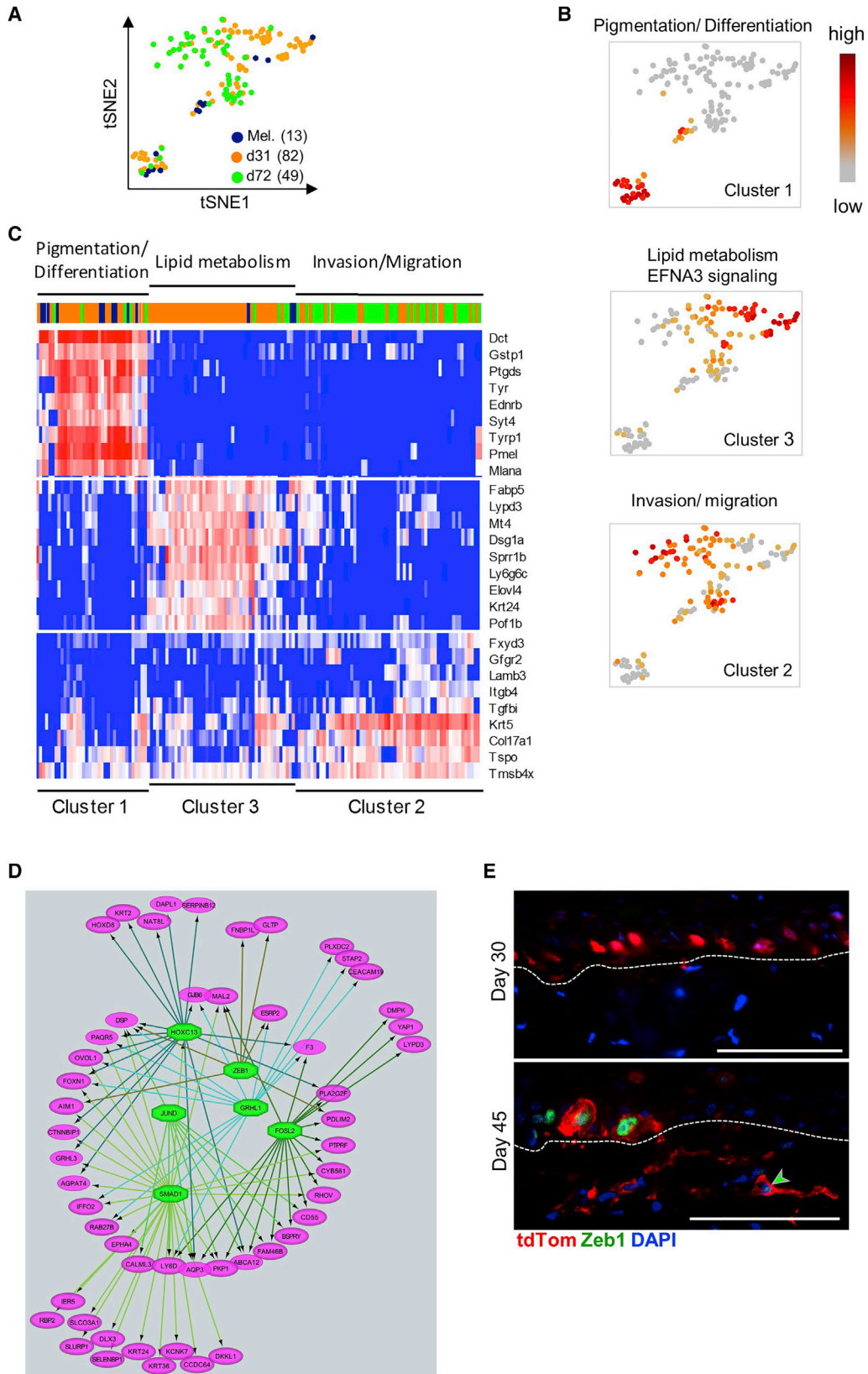
Figure 6. Dermal Invasion Is Accompanied by a Loss Of Expression of Differentiation Markers

(A–C) Immunostaining for E-cadherin (A), gp100 (B), and Mitf (C) in Braf/Pten/tdTomato tail melanoma lesions at the indicated phases of melanoma progression. DAPI nuclear staining is depicted in blue. Scale bars, 50 μ m. Dotted lines mark the epidermal-dermal junction.

1.5–2 months post-4-HT exposure (Figure 2D). The detachment of human melanoma cells from the basal cell layer of the epidermis is thought to be, at least partly, a consequence of loss of E-cadherin expression (Haass et al., 2004; Hsu et al., 1996). Interestingly, we observed a striking decrease in E-cadherin expression in virtually all melanoma cells leaving the mouse tail epidermis and entering the subjacent dermis (Figure 6A). This decrease was accompanied by loss of expression of two well-accepted melanoma differentiation markers, Mitf and gp100 (Figures 6B and 6C), raising the possibility that “dedifferentiation” is concurrent and/or possibly required for dermal invasion.

The Braf/Pten/tdTomato model is therefore well-suited to study the temporal molecular changes that occur in tumor-initiating cells following activation of the melanomagenic program up to when these cells de-differentiate and acquire invasive properties. To this end, we sequenced the transcriptome of fluorescence-activated cell sorting (FACS) individual IFE reporter-positive cells from Braf/Pten/tdTomato mice, the tails of which had been painted with 4-HT for 31 and 72 days, respectively. These time points were chosen as melanoma cells are exclusively found in the IF epidermis at day 31 (d31) and in both epidermis and dermis at day 72 (d72). Normal IF melanocytes from *Tyr::CreER*^{T2/+}; *ROSA26R*^{LSL-tdTomato/+} were also isolated and profiled (Figure S6A). We sequenced 144 individual cells (13 normal melanocytes, 82 epidermal d31 cells, and 49 dermal

d72 melanoma cells) with more than 2,000 transcripts on average per cell. To account for technical noise, we identified highly variable genes (HVGs, $n = 1268$), the expression of which is likely to be driven by biological variation (Figure S6B; Table S1) (Brennecke et al., 2013). Unsupervised clustering based on the expression of these HVGs—using non-negative matrix factorization (NMF) as a dimension reduction approach—identified three distinct subpopulations (Figure S6B). We next tested for significantly differentially expressed genes between these three distinct populations using single-cell differential expression (SCDE) analysis (Kharchenko et al., 2014) and subjected the top 100 ranked genes (Z score, Table S2) of each subpopulation to ingenuity pathway analysis (IPA) (Figure S6B; Tables S3 and S4). IPA indicated that cluster 1 is enriched for cells expressing markers of melanocyte differentiation, pigment/melanin synthesis and downstream targets of the Mitf transcription factor, well-known for its ability to induce pigmentation gene expression and melanocyte differentiation (Levy et al., 2006). Regulatory network analysis using i-Regulon (Janky et al., 2014) confirmed that this particular cluster’s identity is mainly driven by Mitf (Figure S6B). Cluster 3 comprises distinct cells with non-overlapping expression marker genes for lipid metabolism and EphrinA3 (EFNA3) signaling, a pathway previously implicated in melanoma cell proliferation and invasion (Figure S6B) (Janes et al., 2014). Analysis of the regulatory networks at play in these cells



(legend on next page)

predicted an increase activity of Slug (Snai2), an EMT-inducer and master regulator of neural-crest specification and migration (Carver et al., 2001) (Figure S6B). The transcriptome of this cluster is also predicted to be dependent on KLF4 and HOXC13 (Figure S6B). Recent evidence indicated that KLF4 expression is induced in melanoma cells by the RAS/RAF/MEK/ERK signaling pathway and required for cell proliferation and survival (Riverso et al., 2017). A progressive increase in HOXC13 expression during melanoma progression had also previously been reported (Cantile et al., 2012). Cluster 2 has a strong cell invasion/migration identity and pronounced expression of genes downstream of transforming growth factor β (TGF- β)-signaling (Figure S6B). Regulatory landscape analysis identified the AP1 family members Jun and Fos and the TEAD transcription factor, Tead4, as main drivers of this particular cell state (Figure S6B). Interestingly, recent evidence has highlighted a reciprocal antagonism between MITF and c-JUN expression in human melanoma (Riesenberg et al., 2015) and the importance of both AP1 and TEAD transcription factors for the establishment of a melanoma invasive cell state (Verfaillie et al., 2015). Notably, cross-species comparison analysis indicated a significant overlap between clusters 1 and 2 gene expression signatures and the human melanoma “proliferative” and “invasive” gene sets (Verfaillie et al., 2015), respectively. This observation further highlights the human relevance of this refined mouse model (Figure S7).

Visualization of these 3 clusters in two dimensions using *t*-distributed stochastic neighbor embedding (*t*-SNE) revealed that the majority of normal melanocytes clustered with a fraction of the d31 epidermal melanoma cells (Figure 7A). This group of cells expressed the cluster-1 Mitf-driven pigmentation/differentiation signature at the highest levels (Figures 7B and 7C) according to AUCell (Aibar et al., 2017). This observation confirmed the presence of pigment-producing, Mitf-positive, melanoma cells in the epidermis of BRaf/Pten mice at d31 and is consistent with the possibility that these cells originate from pigment-producing founder cells. To further highlight differences between normal melanocytes and d31 melanoma cells of cluster-1, we performed SCDE analysis (Figure S7C). Transcription network analysis on the most differentially expressed genes indicated that the early transformed state of pigmented d31 melanoma cells is driven by Ets-family members, including Etv1 a well-known driver of MAPK-oncogenic signaling (Figure S7D) (Jané-Valbuena et al., 2010).

Cells expressing the cluster-3 signature at high levels were predominantly d31 epidermal melanoma cells (Figures 7A–7C). Most of the d72 dermal melanoma cells, however, expressed predominantly the “invasive-migration” cluster-2 signature. Importantly, these two distinct groups of cells no longer expressed the characteristic melanoma Mitf-induced pigmentation/differentiation markers (Figure 7C). Together, these observations raised the possibility that a subset of epidermal melanoma cells downregulates expression of Mitf and differentiation markers prior to the onset of dermal invasion and before acquiring the characteristic AP1/TEAD-driven invasive phenotype. We performed SCDE and i-Regulon analyses to highlight specific differences between the transformed pigmented cluster-1 and unpigmented cluster-3 d31 melanoma cells (Figure S7E). Among others, we identified Zeb1, a member of the EMT-inducer ZEB family transcription factors, as one of the putative drivers of the unpigmented epidermal cell state. Immunostaining confirmed this prediction (Figure 7E); indeed, whereas many epidermal melanoma cells were Zeb1-negative, Zeb1 expression was readily detectable in a subset of epidermal melanocytes. At day 45, these cells were often located in close proximity to dermal invasion foci and next to dermal Zeb1-positive melanoma cells (Figure 7E). Zeb1 expression was also detected in virtually all d72 dermal melanoma cells (data not shown). These data indicated that loss of differentiation markers occurs in a subset of targeted epidermal melanoma cells before the onset of dermal invasion and that this event may, at least partly, be a consequence of induction of Zeb1 expression.

tion/differentiation markers (Figure 7C). Together, these observations raised the possibility that a subset of epidermal melanoma cells downregulates expression of Mitf and differentiation markers prior to the onset of dermal invasion and before acquiring the characteristic AP1/TEAD-driven invasive phenotype. We performed SCDE and i-Regulon analyses to highlight specific differences between the transformed pigmented cluster-1 and unpigmented cluster-3 d31 melanoma cells (Figure S7E). Among others, we identified Zeb1, a member of the EMT-inducer ZEB family transcription factors, as one of the putative drivers of the unpigmented epidermal cell state. Immunostaining confirmed this prediction (Figure 7E); indeed, whereas many epidermal melanoma cells were Zeb1-negative, Zeb1 expression was readily detectable in a subset of epidermal melanocytes. At day 45, these cells were often located in close proximity to dermal invasion foci and next to dermal Zeb1-positive melanoma cells (Figure 7E). Zeb1 expression was also detected in virtually all d72 dermal melanoma cells (data not shown). These data indicated that loss of differentiation markers occurs in a subset of targeted epidermal melanoma cells before the onset of dermal invasion and that this event may, at least partly, be a consequence of induction of Zeb1 expression.

DISCUSSION

The precise cellular origin of cutaneous melanoma has been a topic of intense debate. To address this critical question, we used lineage-tracing approaches in mice. We induced a melanogenic program, which is driven by the *BRAF*^{V600E}-oncogene and loss of the *Pten* tumor suppressor, in different cell compartments of the melanocytic lineage. We chose to combine these two events because they often co-occur in human melanoma. Importantly, by inducing this oncogenic program in interfollicular (IF) melanocytes located in mouse tails, we created a model that faithfully recapitulates key histopathological features observed in early steps of human melanomagenesis. Using this refined model, we provide evidence that *BRAF*^{V600E}-targeted interfollicular mature, pigment-producing, melanocytes can efficiently serve as the cell of origin of invasive cutaneous melanoma.

In humans, the majority of these cells are located at the dermo-epidermal junction and thereby exposed to UV light. Our findings are therefore consistent with the increasingly recognized role of UV radiation as a driver of melanomagenesis and further emphasize the importance of sun avoidance strategies.

Intriguingly, radial expansion of the BRaf/Pten-targeted melanocytes, which occurred exclusively in the epidermis—just like in human melanoma in situ—proceeded in absence of the loss of differentiation markers, dendritic morphology characteristic of differentiated melanocytes, and the ability to produce melanin.

Figure 7. Single-Cell RNA Sequencing of tdTomato-Positive Cells

- (A) *t*-SNE map showing single normal melanocytes (Mel., blue), d31 (orange), and d72 (green) melanoma cells based on the SCDE and IPA analyses.
 (B) *t*-SNE plot from **a**, with cells colored based on intensity of expression of the 3 pre-defined gene signatures according to AUCell.
 (C) Heatmap displaying discriminative marker genes of cluster 1–3 signatures.
 (D) Regulatory network analysis of differentially expressed genes between pigmented (cluster 1) and unpigmented d31 (cluster 3) melanoma cells identifies Zeb1 as one of the orchestrators of cluster 3.
 (E) Immunostaining for Zeb1 and endogenous expression of tdTomato in BRaf/Pten/tdTomato tail skin at the indicated time points of melanoma progression. The arrow highlights an invading tdTomato-positive melanoma cell. DAPI nuclear staining is depicted in blue. Scale bars, 50 μ m. Dotted lines mark the epidermal-dermal junction.

Consistent with mature melanogenic melanocytes being the cell of origin of these early lesions, the transcriptome of a subset of isolated epidermal melanoma cells clustered with those of normal melanocytes and exhibited the characteristic differentiation, pigment-producing gene expression signature. Although relatively unexpected, this finding is, however, in agreement with previous studies establishing an oncogenic role for MITF-M, a master regulator of melanogenic differentiation (Levy et al., 2006). These data are also entirely consistent with the observation that differentiated melanocytes do cycle, and the human melanoma mutation MITF(4T)(Δ)(2B) promotes increased and serial division of differentiated melanocytes in zebrafish (Taylor et al., 2011).

Following this first phase of radial expansion, a subset of epidermal melanoma cells undergoes a profound transcriptional reprogramming that is characterized by loss of the MITF-driven expression signature. This “dedifferentiation” process may be reminiscent to the observation that reemergence of a dedifferentiated neural-crest progenitor state is required for the formation of melanoma in an elegant zebrafish model (Kaufman et al., 2016). Interestingly, dedifferentiation of mouse epidermal melanoma cells occurs prior to the onset of dermal invasion. What is triggering this event remains unclear. Because it occurs at a stage when the epidermis is literally filled up with packed melanoma cells, one hypothesis is that nutrients, such as keratinocyte-produced growth factors, become limited. As recently proposed (Falletta et al., 2017), this phenotype switch may thus be due to activation of a starvation-stress response and metabolic rewiring. Consistent with the latter, concomitant to the loss of the MITF-driven gene expression signature induction, we observed an enrichment of expression of genes involved in lipid metabolism. Our regulatory landscape analysis, however, failed to identify Atf4 as a putative driver of this phenotype switch. The Atf4 transcription factor has recently been implicated as a key mediator of an evolutionarily conserved starvation-response that promotes phenotypic plasticity and melanoma cell invasion (Falletta et al., 2017). Instead, we identified Zeb1 and AP1 transcription factors as putative orchestrators of the epidermal phenotype switch observed during early progression of the mouse tail melanoma lesions.

Interestingly, a second phenotype switching event was identified as these lesions progressed further and eventually invaded the underlying dermis. Interestingly, GSEA highlighted a significant overlap between the transcriptome of the BRAF/Pten-targeted dermal mouse melanoma cells and the characteristic gene expression signature of human invasive melanoma cells described previously (Verfaillie et al., 2015). Both mouse and human transcriptional programs appear to be driven by the same transcription factors, namely AP1 and TEADs. These data further emphasize the clinical relevance of this refined mouse melanoma model and its suitability to dissect the molecular mechanisms underlying the early steps of human melanomagenesis. The model will be particularly valuable to study the histogenetic subtypes that develop according to a biphasic growth pattern, such as superficial spreading, lentigo maligna, and acral lentiginous melanomas. Note that, in contrast, the model is not appropriate to study the development of nodular melanoma, a type of melanoma that appears suddenly with no apparent precursor and that may have its origin in dermally located cells.

Strikingly, interfollicular immature/amelanotic melanocytes, which we show are dormant cells residing in the interscale hinges, were tumor-resistant. Similarly, we also provide evidence that amelanotic MSCs, which reside in the HF bulge, are incompetent to initiate melanoma formation within their niche. This observation seemingly contrasts with evidence that resident adult stem cells are the cells of origin of many different tumor types (White and Lowry, 2015). It also somewhat contrasts with the view that MSCs may be at the origin of cutaneous melanoma, a hypothesis that emerged following the discovery of melanocyte and melanoma stem cells. It has been proposed that the growth of human melanoma is driven by a small subpopulation of melanoma stem cells that can be distinguished from nontumorigenic melanoma cells by the expression of ABCB5 (Schattton et al., 2008) or CD271 (Boiko et al., 2010), and these cells may derive from the transformation of a MSC. It is important to emphasize that although we provide evidence that mature pigment-producing cells can serve as the cells of origin, our studies do not exclude the possibility that MSCs can also contribute. First, although we and others have demonstrated that the *Tyr::CreER*^{T2} transgenic line used in this study efficiently drives Cre-dependent locus recombination in the MSC compartment (Bosenberg et al., 2006; Harris and Pavan, 2013; Harris et al., 2013), our conclusions would benefit from future studies using independent technical tools that do not rely upon a Cre that is driven from a pigment gene promoter. Second, it is entirely possible that melanoma, being a heterogeneous collection of diseases (Shain and Bastian, 2016), may arise from multiple cell types of origin. For instance, it remains possible that the cell of origin of nodular melanoma is a dermally located resident (and/or neural crest) stem cell. Third, we actually show that oncogene-targeted HF bulge MSCs are tumor-resistant within their niche but can promote tumor formation after exiting the bulge and migrating down to the matrix as mature, pigment-producing cells. These targeted progenies eventually resume cell proliferation and contribute to clonal expansion within the matrix. Vice versa, we also show that although pigmented melanocytes are present in the interscale hinges, these cells display very limited to no-tumor-initiating capacity. Together, these data demonstrate that both amelanotic and melanogenic melanocytes have the intrinsic capacity to function as tumor initiating cells, but whether or not they do is dictated by the microenvironment in which they reside. Our studies demonstrate that the niches that support the dormancy of amelanotic melanocytes (i.e., HF bulge and tail interscale) strongly inhibit melanoma initiation. Further work will be required to identify the factors that contribute to the tumor-modulator’s role of these niches and whether targeting these niche factors might represent a viable therapeutic strategy.

Although many tumors contain cells that display stem cell-like features, the identity of the normal cells that acquire the first genetic “hits” that lead to tumor initiation has remained elusive. Whereas there is an increasing body of evidence that cancer-initiating cells can derive from resident adult tissue stem cells (White and Lowry, 2015) whether mature cells can undergo a de-differentiation or transdifferentiation process is still unclear. Experiments in vitro have suggested that differentiated cells can give rise to cancer. These data indicated that fully differentiated cells, under certain conditions, are able to de-differentiate

into cancer-initiating cells. However, this possibility has never been challenged by *in vivo* experiments in which oncogenes are expressed at physiological levels. Critically, our data provide the first direct *in vivo* demonstration that normal somatic cells that are fully differentiated can be reprogrammed into cancer-initiating cells. This finding raises the possibility that other cancers may also have their earliest beginnings in a fully differentiated cell.

STAR★METHODS

Detailed methods are provided in the online version of this paper and include the following:

- KEY RESOURCES TABLE
- CONTACT FOR REAGENT AND RESOURCE SHARING
- EXPERIMENTAL MODEL AND SUBJECT DETAILS
 - Mice
 - Mouse treatments
- METHOD DETAILS
 - Epidermal whole mount
 - Histopathology and immunohistochemistry
 - Immunofluorescence with tyramide signal amplification
 - Immunofluorescence on frozen sections
 - Microscope image acquisition
 - Live *in vivo* Imaging
 - Preparation of single cell suspensions
 - Flow cytometry
 - Recombination PCR
 - Single Cell RNA-Seq and data analysis
- QUANTIFICATION AND STATISTICAL ANALYSIS
 - Quantification of melanocyte number
 - Quantification of clone size
- DATA AND SOFTWARE AVAILABILITY

SUPPLEMENTAL INFORMATION

Supplemental Information includes seven figures and four tables and can be found with this article online at <https://doi.org/10.1016/j.stem.2017.08.003>.

AUTHOR CONTRIBUTIONS

C.K. and D.N. designed and conducted experiments and acquired, analyzed, and interpreted the data. E.R. and J.v.d.O. provided mouse and human pathology support. F.S. and H.G. provided intravital imaging expertise and support. J.v.d.O. provided valuable clinical samples. C.B., N.V., and G.B. provided valuable reagents and contributed to interpretation of the data. All authors read and edited the manuscript. J.-C.M. designed research studies and wrote the manuscript.

ACKNOWLEDGMENTS

We thank O. Van Goethem, G. Bervoets, and S. Peeters for excellent technical assistance; Hans Clevers for providing us with the Confetti-reporter mouse strain; and Koen Theunis, Thierry Voet, Sara Santos, and Stein Aerts for their precious help with the single-cell transcriptomic experiments and bioinformatics analysis. This work was supported in part by the Fund for Scientific Research Flanders (FWO; G.0664.14), Interuniversitaire Attractiepolen (IUAP, Belspo P7/03), Stichting tegen Kanker (STK 2014-126), a Hercules type 2 research infrastructure grant (to H.G.), and FWO Ph.D. and postdoctoral fellowships to C.K. (11Y9715N, 11Y9717N) and D.N. (12D3214N), respectively.

H.G. and F.S. were supported by the European Research Council (consolidator grant 311719 REshape).

Received: March 18, 2017

Revised: June 28, 2017

Accepted: August 9, 2017

Published: October 12, 2017

REFERENCES

- Aibar, S., Bravo González-Blas, C., Moerman, T., Wouters, J., Huynh-Thu, V.A., Imrichová, H., Kalender Atak, Z., Hulselmans, G., Dewaele, M., Rambow, F., et al. (2017). SCENIC: single-cell regulatory network inference and clustering. *bioRxiv*. <https://doi.org/10.1101/144501>.
- Anders, S., and Huber, W. (2010). Differential expression analysis for sequence count data. *Genome Biol.* *11*, R106.
- Balch, C.M., Buzaid, A.C., Soong, S.J., Atkins, M.B., Cascinelli, N., Coit, D.G., Fleming, I.D., Gershenwald, J.E., Houghton, A., Jr., Kirkwood, J.M., et al. (2001). Final version of the American Joint Committee on Cancer staging system for cutaneous melanoma. *J. Clin. Oncol.* *19*, 3635–3648.
- Boiko, A.D., Razorenova, O.V., van de Rijn, M., Swetter, S.M., Johnson, D.L., Ly, D.P., Butler, P.D., Yang, G.P., Joshua, B., Kaplan, M.J., et al. (2010). Human melanoma-initiating cells express neural crest nerve growth factor receptor CD271. *Nature* *466*, 133–137.
- Bosenberg, M., Muthusamy, V., Curley, D.P., Wang, Z., Hobbs, C., Nelson, B., Nogueira, C., Horner, J.W., 2nd, Depinho, R., and Chin, L. (2006). Characterization of melanocyte-specific inducible Cre recombinase transgenic mice. *Genesis* *44*, 262–267.
- Brennecke, P., Anders, S., Kim, J.K., Kołodziejczyk, A.A., Zhang, X., Proserpio, V., Baying, B., Benes, V., Teichmann, S.A., Marioni, J.C., and Heisler, M.G. (2013). Accounting for technical noise in single-cell RNA-seq experiments. *Nat. Methods* *10*, 1093–1095.
- Cantile, M., Scognamiglio, G., Anniciello, A., Farina, M., Gentile, G., Santonastaso, C., Fulciniti, F., Cillo, C., Franco, R., Ascierto, P.A., and Botti, G. (2012). Increased HOX C13 expression in metastatic melanoma progression. *J. Transl. Med.* *10*, 91.
- Carver, E.A., Jiang, R., Lan, Y., Oram, K.F., and Gridley, T. (2001). The mouse snail gene encodes a key regulator of the epithelial-mesenchymal transition. *Mol. Cell. Biol.* *21*, 8184–8188.
- Chou, W.C., Takeo, M., Rabbani, P., Hu, H., Lee, W., Chung, Y.R., Carucci, J., Overbeek, P., and Ito, M. (2013). Direct migration of follicular melanocyte stem cells to the epidermis after wounding or UVB irradiation is dependent on Mc1r signaling. *Nat. Med.* *19*, 924–929.
- Chu, V.T., Gottardo, R., Raftery, A.E., Bumgarner, R.E., and Yeung, K.Y. (2008). MeV+R: using MeV as a graphical user interface for Bioconductor applications in microarray analysis. *Genome Biol.* *9*, R118.
- Clark, W.H., Jr., Ainsworth, A.M., Bernardino, E.A., Yang, C.H., Mihm, C.M., Jr., and Reed, R.J. (1975). The developmental biology of primary human malignant melanomas. *Semin. Oncol.* *2*, 83–103.
- Damsky, W.E., Curley, D.P., Santhanakrishnan, M., Rosenbaum, L.E., Platt, J.T., Gould Rothberg, B.E., Taketo, M.M., Dankort, D., Rimm, D.L., McMahon, M., and Bosenberg, M. (2011). β -catenin signaling controls metastasis in Braf-activated Pten-deficient melanomas. *Cancer Cell* *20*, 741–754.
- Dankort, D., Filenova, E., Collado, M., Serrano, M., Jones, K., and McMahon, M. (2007). A new mouse model to explore the initiation, progression, and therapy of BRAFV600E-induced lung tumors. *Genes Dev.* *21*, 379–384.
- Di Girolamo, N., Bobba, S., Raviraj, V., Delic, N.C., Slapetova, I., Nicovich, P.R., Halliday, G.M., Wakefield, D., Whan, R., and Lyons, J.G. (2015). Tracing the fate of limbal epithelial progenitor cells in the murine cornea. *Stem Cells* *33*, 157–169.
- Didierjean, L., Wrench, R., and Saurat, J.H. (1983). Expression of cytoplasmic antigens linked to orthokeratosis during the development of parakeratosis in newborn mouse tail epidermis. *Differentiation* *23*, 250–255.

- Dobin, A., Davis, C.A., Schlesinger, F., Drenkow, J., Zaleski, C., Jha, S., Batut, P., Chaisson, M., and Gingeras, T.R. (2013). STAR: ultrafast universal RNA-seq aligner. *Bioinformatics* 29, 15–21.
- Falletta, P., Sanchez-Del-Campo, L., Chauhan, J., Effern, M., Kenyon, A., Kershaw, C.J., Siddaway, R., Lisle, R., Freter, R., Daniels, M.J., et al. (2017). Translation reprogramming is an evolutionarily conserved driver of phenotypic plasticity and therapeutic resistance in melanoma. *Genes Dev.* 31, 18–33.
- Glover, J.D., Knolle, S., Wells, K.L., Liu, D., Jackson, I.J., Mort, R.L., and Headon, D.J. (2015). Maintenance of distinct melanocyte populations in the interfollicular epidermis. *Pigment Cell Melanoma Res.* 28, 476–480.
- Haass, N.K., Smalley, K.S.M., and Herlyn, M. (2004). The role of altered cell-cell communication in melanoma progression. *J. Mol. Histol.* 35, 309–318.
- Harris, M.L., and Pavan, W.J. (2013). Postnatal lineage mapping of follicular melanocytes with the Tyr:CreER(T) (2) transgene. *Pigment Cell Melanoma Res.* 26, 269–274.
- Harris, M.L., Buac, K., Shakhova, O., Hakami, R.M., Wegner, M., Sommer, L., and Pavan, W.J. (2013). A dual role for SOX10 in the maintenance of the postnatal melanocyte lineage and the differentiation of melanocyte stem cell progenitors. *PLoS Genet.* 9, e1003644.
- Hoerter, J.D., Bradley, P., Casillas, A., Chambers, D., Weiswasser, B., Clements, L., Gilbert, S., and Jiao, A. (2012). Does melanoma begin in a melanocyte stem cell? *J. Skin Cancer* 2012, 571087.
- Hsu, M.Y., Wheelock, M.J., Johnson, K.R., and Herlyn, M. (1996). Shifts in cadherin profiles between human normal melanocytes and melanomas. *J. Investig. Dermatol. Symp. Proc.* 1, 188–194.
- Hsu, Y.-C., Pasolli, H.A., and Fuchs, E. (2011). Dynamics between stem cells, niche, and progeny in the hair follicle. *Cell* 144, 92–105.
- Jané-Valbuena, J., Widlund, H.R., Perner, S., Johnson, L.A., Dibner, A.C., Lin, W.M., Baker, A.C., Nazarian, R.M., Vijayendran, K.G., Sellers, W.R., et al. (2010). An oncogenic role for ETV1 in melanoma. *Cancer Res.* 70, 2075–2084.
- Janes, P.W., Slape, C.I., Farnsworth, R.H., Atapattu, L., Scott, A.M., and Vail, M.E. (2014). EphA3 biology and cancer. *Growth Factors* 32, 176–189.
- Janky, R., Verfaillie, A., Imrichová, H., Van de Sande, B., Standaert, L., Christiaens, V., Hulselmans, G., Herten, K., Naval Sanchez, M., Potier, D., et al. (2014). iRegulon: from a gene list to a gene regulatory network using large motif and track collections. *PLoS Comput. Biol.* 10, e1003731.
- Kaufman, C.K., Mosimann, C., Fan, Z.P., Yang, S., Thomas, A.J., Ablain, J., Tan, J.L., Fogley, R.D., van Rooijen, E., Hagedorn, E.J., et al. (2016). A zebrafish melanoma model reveals emergence of neural crest identity during melanoma initiation. *Science* 351, aad2197.
- Kharchenko, P.V., Silberstein, L., and Scadden, D.T. (2014). Bayesian approach to single-cell differential expression analysis. *Nat. Methods* 11, 740–742.
- Lesche, R., Groszer, M., Gao, J., Wang, Y., Messing, A., Sun, H., Liu, X., and Wu, H. (2002). Cre/loxP-mediated inactivation of the murine Pten tumor suppressor gene. *Genesis* 32, 148–149.
- Levy, C., Khaled, M., and Fisher, D.E. (2006). MITF: master regulator of melanocyte development and melanoma oncogene. *Trends Mol. Med.* 12, 406–414.
- Madisen, L., Zwingman, T.A., Sunkin, S.M., Oh, S.W., Zariwala, H.A., Gu, H., Ng, L.L., Palmiter, R.D., Hawrylycz, M.J., Jones, A.R., et al. (2010). A robust and high-throughput Cre reporting and characterization system for the whole mouse brain. *Nat. Neurosci.* 13, 133–140.
- Mascre, G., Dekoninck, S., Drogat, B., Youssef, K.K., Brohee, S., Sotiropoulou, P.A., Simons, B.D., and Blanpain, C. (2012). Distinct contribution of stem and progenitor cells to epidermal maintenance. *Nature* 489, 257–262.
- Mort, R.L., Jackson, I.J., and Patton, E.E. (2015). The melanocyte lineage in development and disease. *Development* 142, 1387.
- Müller-Röver, S., Handjiski, B., van der Veen, C., Eichmüller, S., Foitzik, K., McKay, I.A., Stenn, K.S., and Paus, R. (2001). A comprehensive guide for the accurate classification of murine hair follicles in distinct hair cycle stages. *J. Invest. Dermatol.* 117, 3–15.
- Nishimura, E.K. (2011). Melanocyte stem cells: a melanocyte reservoir in hair follicles for hair and skin pigmentation. *Pigment Cell Melanoma Res.* 24, 401–410.
- Nishimura, E.K., Jordan, S.A., Oshima, H., Yoshida, H., Osawa, M., Moriyama, M., Jackson, I.J., Barrandon, Y., Miyachi, Y., and Nishikawa, S. (2002). Dominant role of the niche in melanocyte stem-cell fate determination. *Nature* 416, 854–860.
- Picelli, S., Faridani, O.R., Björklund, A.K., Winberg, G., Sagasser, S., and Sandberg, R. (2014). Full-length RNA-seq from single cells using Smart-seq2. *Nat. Protoc.* 9, 171–181.
- Preibisch, S., Saalfeld, S., and Tomancak, P. (2009). Globally optimal stitching of tiled 3D microscopic image acquisitions. *Bioinformatics* 25, 1463–1465.
- Riesenberg, S., Groetchen, A., Siddaway, R., Bald, T., Reinhardt, J., Smorra, D., Kohlmeyer, J., Renn, M., Phung, B., Aymans, P., et al. (2015). MITF and c-Jun antagonism interconnects melanoma dedifferentiation with pro-inflammatory cytokine responsiveness and myeloid cell recruitment. *Nat. Commun.* 6, 8755.
- Rivero, M., Montagnani, V., and Stecca, B. (2017). KLF4 is regulated by RAS/RAF/MEK/ERK signaling through E2F1 and promotes melanoma cell growth. *Oncogene* 36, 3322–3333.
- Schatton, T., Murphy, G.F., Frank, N.Y., Yamaura, K., Waaga-Gasser, A.M., Gasser, M., Zhan, Q., Jordan, S., Duncan, L.M., Weishaupt, C., et al. (2008). Identification of cells initiating human melanomas. *Nature* 451, 345–349.
- Schweizer, J., and Marks, F. (1977). A developmental study of the distribution and frequency of Langerhans cells in relation to formation of patterning in mouse tail epidermis. *J. Invest. Dermatol.* 69, 198–204.
- Shain, A.H., and Bastian, B.C. (2016). From melanocytes to melanomas. *Nat. Rev. Cancer* 16, 345–358.
- Srinivas, S., Watanabe, T., Lin, C.S., Williams, C.M., Tanabe, Y., Jessell, T.M., and Costantini, F. (2001). Cre reporter strains produced by targeted insertion of EYFP and ECFP into the ROSA26 locus. *BMC Dev. Biol.* 1, 4.
- Taylor, K.L., Lister, J.A., Zeng, Z., Ishizaki, H., Anderson, C., Kelsh, R.N., Jackson, I.J., and Patton, E.E. (2011). Differentiated melanocyte cell division occurs in vivo and is promoted by mutations in Mitf. *Development* 138, 3579–3589.
- Tirosh, I., Izar, B., Prakadan, S.M., Wadsworth, M.H., Treacy, D., Trombetta, J.J., Rotem, A., Rodman, C., Lian, C., Murphy, G., et al. (2016). Dissecting the multicellular ecosystem of metastatic melanoma by single-cell RNA-seq. *Science* 352, 189–196.
- Tumbar, T., Guasch, G., Greco, V., Blanpain, C., Lowry, W.E., Rendl, M., and Fuchs, E. (2004). Defining the epithelial stem cell niche in skin. *Science* 303, 359–363.
- Verfaillie, A., Imrichová, H., Atak, Z.K., Dewaele, M., Rambow, F., Hulselmans, G., Christiaens, V., Svetlichnyy, D., Luciani, F., Van den Mooter, L., et al. (2015). Decoding the regulatory landscape of melanoma reveals TEADS as regulators of the invasive cell state. *Nat. Commun.* 6, 6683.
- Waghmare, S.K., Bansal, R., Lee, J., Zhang, Y.V., McDermitt, D.J., and Tumbar, T. (2008). Quantitative proliferation dynamics and random chromosome segregation of hair follicle stem cells. *EMBO J.* 27, 1309–1320.
- White, A.C., and Lowry, W.E. (2015). Refining the role for adult stem cells as cancer cells of origin. *Trends Cell Biol.* 25, 11–20.
- Zaidi, M.R., Hornyak, T.J., and Merlino, G. (2011). A genetically engineered mouse model with inducible GFP expression in melanocytes. *Pigment Cell Melanoma Res.* 24, 393–394.

STAR★METHODS

KEY RESOURCES TABLE

REAGENT or RESOURCE	SOURCE	IDENTIFIER
Antibodies		
Rabbit monoclonal anti-Melanoma gp100	abcam	Cat#ab137078
Rabbit polyclonal anti-K10	BioLegend	Cat#905401 RRID: AB_2565049
Rabbit monoclonal anti-Ki67	Thermoscientific	Cat#RM-9106 RRID: AB_2335745
Rabbit polyclonal anti-S100	DAKO	Cat#Z0311 RRID: AB_10013383
Goat polyclonal anti-GFP	abcam	Cat#ab6673 RRID: AB_305643
Rabbit polyclonal anti-Zeb1	Santa Cruz	Cat#sc-25388 RRID: AB_2217979
Rabbit monoclonal anti-phospho-Akt (Ser473)	Cell Signaling Technology	Cat#4060 RRID: AB_2315049
Rabbit monoclonal anti- Phospho-p44/42 MAPK (Erk1/2) (Thr202/Tyr204) (D13.14.4E) XP(tm)	Cell Signaling Technology	Cat#4370 RRID: AB_2315112
Chemicals, Peptides, and Recombinant Proteins		
4-Hydroxytamoxifen \geq 70% Z isomer	Sigma-Aldrich	Cat#H6278 CAS: 68392-35-8
Dimethyl sulfoxide (DMSO)	Sigma-Aldrich	Cat#276855 CAS: 67-68-5
Nimatek (100mg/ml)	eurovet	BE-V439546
Rompun2%	BAYER	BE-V170581
Gum rosin	Sigma-Aldrich	Cat#60895 CAS: 8050-09-7
Beeswax	Sigma-Aldrich	Cat#243248 CAS: 8012-89-3
Doxycycline (Dox)	Sigma-Aldrich	Cat#D9891 CAS: 24390-14-5
Ethylenediaminetetraacetic acid disodium salt dihydrate (EDTA)	Sigma-Aldrich	Cat#E6635 CAS: 6381-92-6
Dulbecco's Phosphate Buffered Saline (PBS)	Sigma-Aldrich	Cat#D8537
Paraformaldehyde (PFA)	Sigma-Aldrich	Cat# 158127 CAS: 30525-89-4
Bovine Serum Albumin (BSA)	Sigma-Aldrich	Cat#A9647 CAS: 9048-46-8
Donkey Serum	Sigma-Aldrich	Cat# D9663
Tween 20	VWR	Cat# 0777 CAS: 9005-64-5
DAPI (4',6-Diamidino-2-Phenylindole, Dihydrochloride)	Thermo Fisher Scientific	Cat# 62247 CAS: 28718-90-3
DAPI (4',6-Diamidino-2-Phenylindole, Dihydrochloride)	Sigma-Aldrich	Cat# D9542 CAS: 28718-90-3
VECTASHIELD Antifade Mounting Medium	Vector Laboratories	Cat# H-1000
Triton X-100	Sigma-Aldrich	Cat# T8787 CAS: 9002-93-1
Hydrogen peroxide solution	Sigma-Aldrich	Cat# 216763 CAS: 7722-84-1
Micromount	Diapath	Cat# 060200
Mowiol 4-88	Sigma-Aldrich	Cat# 81381 CAS: 9002-89-5
Tissue-Tek O.C.T. TM Compound	Sakura	Cat# 4583
Collagenase type I	Sigma-Aldrich	Cat# SCR103
Collagenase type IV	Sigma-Aldrich	Cat# C5138
Trypsin (0.25%)	Thermo Scientific Fisher	Cat# 25200056
Fetal Calf Serum (FCS)	Thermo Scientific Fisher	Cat# 10270106
10x Hanks' Balanced Salt Solution (HBSS)	Thermo Scientific Fisher	Cat# 14065056
KAPA HiFi Hot start Readymix	Sopachem	KK2602
Agencourt AMPure XP beads	Agencourt/ Beckman coulter	A63881
Superscript II	Fisher Scientific	10328062
Critical Commercial Assays		
QIAamp DNA Micro Kit	QIAGEN	Cat# 56304
RedTaq DNA Polymerase Master Mix	VWR	Cat# 733-2546

(Continued on next page)

Continued

REAGENT or RESOURCE	SOURCE	IDENTIFIER
VECTASTAIN Elite ABC HRP Kit	Vector Laboratories	Cat# PK-6100
ImmPACT DAB Peroxidase (HRP) Substrate	Vector Laboratories	Cat# SK-4105
Dako AEC+ High Sensitivity Substrate Chromogen	Dako	Cat# K3461
Opal 4-Color Manual IHC Kit 50 slides	PerkinElmer	Cat# NEL810001KT
EnVision+ Single Reagents, HRP. Rabbit	Dako	Cat# K400311-2
Nextera XT library Prep Kit	Illumina	FC-131-1096
Nextera XT Index Kit v2 Set A	Illumina	FC-131-2001
Nextera XT Index Kit v2 Set B	Illumina	FC-131-2002
Nextera XT Index Kit v2 Set C	Illumina	FC-131-2003
Nextera XT Index Kit v2 Set D	Illumina	FC-131-2004
Deposited Data		
Raw and analyzed data	This paper	GEO: GSE100607
Experimental Models: Organisms/Strains		
Mouse: B6.Cg-Tg(Tyr-cre/ERT2)13Bos/J (Tyr::CreER ^{T2})	The Jackson Laboratory	012328
Mouse: B6.129P2(Cg)-Braf ^{tm1Mmcm} /J (BRaf ^{CA})	The Jackson Laboratory	017837
Mouse: C;129S4-Pten ^{tm1Hwu} /J (Pten ^{l/l})	The Jackson Laboratory	004597
Mouse: B6.129X1-Gt(ROSA)26Sor ^{tm1(EYFP)Cos} /J (ROSA26R ^{LSL-YFP})	The Jackson Laboratory	006148
Mouse: B6;129S6-Gt(ROSA)26Sor ^{tm9(CAG-tdTomato)Hze} /J (ROSA26R ^{LSL-tdTomato})	The Jackson Laboratory	007905
Mouse: Gt(ROSA)26Sor ^{tm1(CAG-Brainbow2.1)Cle} /J (ROSA26R ^{LSL-Confetti})	The Jackson Laboratory	013731
Mouse: FVB.Cg-Tg(Dct-rtTA2S*M2)#Mrln Tg(tetO-HIST1H2BJ/GFP)47Efu/Nci (iDct-GFP)	NCI Mouse Repository	01XT4
Oligonucleotides		
Primer: recombination PCR Pten	(Lesche et al., 2002)	N/A
Fwd: 5'-ACTCAAGGCAGG-GATGAGC-3'	(Lesche et al., 2002)	N/A
Rev1: 5'-AATCTAGGGCCTCTGTG CC-3	(Lesche et al., 2002)	N/A
Rev2: 5'-GCTTGATATCGAATTCCTGCAGC-3'	(Lesche et al., 2002)	N/A
Primer: recombination PCR Braf	(Dankort et al., 2007)	N/A
Fwd: 5'-TGAGTATTTTGTGGCAACTGC-3	(Dankort et al., 2007)	N/A
Rev: 5'-CTCTGCTGGAAAGCGGC-3'	(Dankort et al., 2007)	N/A
Software and Algorithms		
DESeq2	(Anders and Huber, 2010)	https://bioconductor.org/packages/release/bioc/html/DESeq2.html
SCENIC	(Aibar et al., 2017)	https://github.com/aertslab/SCENIC
MeV (4.8 Version 10.2)	(Chu et al., 2008)	http://www.tm4.org/
SCDE (2.4.1)	(Kharchenko et al., 2014)	https://bioconductor.org/packages/release/bioc/html/scde.html
GraphPad Prism 7	GraphPad Software, Inc	https://www.graphpad.com/scientific-software/prism/
STAR RNaseq mapping	(Dobin et al., 2013)	https://github.com/alexdobin/STAR/releases

CONTACT FOR REAGENT AND RESOURCE SHARING

Additional information and requests for reagents may be directed to and will be fulfilled by the Lead Contact, Jean-Christophe Marine (jeanchristophe.marine@kuleuven.vib.be).

EXPERIMENTAL MODEL AND SUBJECT DETAILS

Mice

Mice carrying the transgenic alleles *Tyr::CreERT2*, *BRAF^{CA/+}*, *Pten^{fl/fl}*, *R26R^{LSL-eYFP}*, *R26R^{LSL-confetti}*, *R26R^{LSL-tdTomato}*, *Dct-rtTA* and *iDct-GFP* have been described previously (Bosenberg et al., 2006; Dankort et al., 2007; Di Girolamo et al., 2015; Madisen et al., 2010; Srinivas et al., 2001; Zaidi et al., 2011). Mice were bred and crossed in-house to generate *Tyr::CreER^{T2/+}*, *BRAF^{CA/+}*, *Pten^{fl/fl}*, *ROSA26R^{LSL-YFP/+}*, *Tyr::CreER^{T2/+}*, *BRAF^{CA/+}*, *Pten^{fl/fl}*, *ROSA26R^{LSL-tdTomato/+}* and *Tyr::CreER^{T2/+}*, *BRAF^{CA/+}*, *Pten^{fl/fl}*, *ROSA26R^{LSL-confetti/LSL-confetti}* mice. iDct-GFP mice were originally purchased from NCI Mouse Repository (Frederick, MD), backcrossed to C57BL/6J and bred in-house.

Mouse treatments

Topical administration of 4-hydroxytamoxifen (4-HT) was conducted by preparing a 50mg/ml solution (130mM) of 4-HT (70% Z-isomer, Sigma) in dimethylsulfoxide (DMSO). For localized melanoma induction on the back of *Tyr::CreER^{T2/+}*, *BRAF^{CA/+}*, *Pten^{fl/fl}* mice, 7 weeks-old mice were anesthetized with Ketamin (NIMATEK 100mg/ml, eurovet) and Xylazine (Rompun®2%, BAYER) and depilated from a ca. 2x3cm patch of skin on the back with a combination of gum rosin and bee wax (Sigma). 6µl of the 4-HT solution was applied on a defined area of 1.5x1.5cm on the depilated back skin either directly or 5 days after depilation. For distal melanoma induction on the tail, 1µl per cm tail (length) of 130mM 4-HT was applied. Tails were wrapped subsequently using Tegaderm™ Transparent Film Dressing to avoid spreading of 4-HT. All treated mice were evaluated twice weekly for tumor appearance and progression. Mice were dissected on defined time points or before tumors reached 15mm³. The treatment of iDct-GFP bi-transgenic mice had been described earlier (Zaidi et al., 2011). Adult mice were injected i.p. with a single non-toxic dose (80µg/g body weight) of doxycycline (Sigma) diluted in PBS. All experiments involving animals were reviewed and approved by the University of Leuven Animal Care and Use ethical committee. Animals were housed and bred according to institutional guidelines. Specifically, animals were housed in a controlled environment with 14/10hour light/dark cycles, standard diet and water ad libitum.

METHOD DETAILS

Epidermal whole mount

The protocol was adapted from Mascré et al., (2012). Murine tail skin was dissected and spread out on Whatman® cellulose filter paper. Pieces of murine tail skin were cut and incubated in 20mM EDTA in PBS at 37°C for 40min in the dark and washed twice with PBS subsequently. The epidermis was mechanically separated from the dermis as an intact sheet and was fixed in 4% paraformaldehyde for 30min at room temperature (RT) in the dark. Pieces of Epidermis were rinsed twice with PBS and stored at 4°C or immediately processed for the antibody staining. Pieces of epidermis were incubated in blocking buffer (1%BSA, 10% donkey serum, 0.2% Tween in PBS) for 3h at RT on a rocking plate (120rpm) in the dark. Blocked samples were incubated in primary antibodies diluted in antibody diluent (1%BSA, 0.2% tween in PBS) overnight at 4°C in the dark. The primary antibodies used were anti-Melanoma gp100 (rabbit, 1:400, abcam, ab137078), anti-K10 (rabbit, 1:2000, BioLegend, 905401) and anti-Ki67 clone SP6 (rabbit, 1:200, ThermoFisher, RM-9106). Samples were then washed three times in PBS with 0.2% tween for 1h and incubated in appropriate secondary antibodies diluted 1:400 in antibody diluent for 2h at RT on a rocking plate in the dark. Nuclei were stained with DAPI solution (0.5mg/ml) diluted 1:1000 in PBS for 20min and mounted in VECTASHIELD® Antifade Mounting Medium for fluorescence (VECTOR).

Histopathology and immunohistochemistry

Tissue samples from representative lesions were collected and fixed in 4% paraformaldehyde for 24 hr and then processed for paraffin embedding (Thermo Scientific Excelsior AS Tissue Processor and HistoStar Embedding Workstation). Sections of 5 µm of thickness obtained from the paraffin-embedded tissues (Thermo Scientific Microm HM355S microtome) were mounted on Superfrost Plus Adhesion slides (Thermo Scientific) and routinely stained with hematoxylin and eosin (H&E, Diapath #C0302 and #C0362) for histopathological examination. Immunofluorescence and/or immunoperoxidase stain was performed on paraffin sections using the following antibodies: anti-gp100 (rabbit, 1:400, abcam, ab137078), anti-S100 (rabbit, 1:2000, DAKO, Z0311), anti-YFP (goat, 1:400, abcam, ab6673), anti-Zeb1 (rabbit, 1:200, Santa Cruz, sc-25388). Briefly, slides were deparaffinized in xylene and then rehydrated in ethanol series (100%, 95%, and 70%) and distilled water. Inhibition of endogenous peroxidase was achieved incubating the slides in 3% hydrogen peroxide for 15 min at RT. Epitope retrieval was performed in citrate buffer (pH6) using the 2100 Retriever. Sections were blocked in 1% BSA solution for 40 min at RT and then incubated overnight at 4°C with the primary antibody. For the immunoperoxidase technique, the EnVision+HRP reagent or Avidin-Biotin Complex (Vector Labs, Vectastain Elite ABC kit PK-6100) system was used according to the manufacturer's protocol. Immunoreactivity was finally revealed via diaminobenzidine (Vector Labs ImmPACT DAB SK-4105Peroxidase substrate kit, DAB, SK-4100) or 3-amino-9-ethylcarbazole (Dako AEC+ Code K3461) chromogen reaction. Slides were counterstained in hematoxylin, dehydrated in ethanol series, cleared in xylene, and permanently mounted with a resinous mounting medium (Micromount Diapath, #60200). For immunofluorescence, DAPI (Sigma-Aldrich D9542) was used as nuclear counterstain and the slides were mounted with Mowiol® (Sigma #324590). A 0.1% Tween 20 TBS solution was used as washing buffer in between steps.

Immunofluorescence with tyramide signal amplification

For detecting p-Akt and p-Erk paraffin sections were used with the following antibodies: anti-Phospho-Akt (Ser473) (D9E) (rabbit, 1:300, Cell Signaling, 4060), anti-Phospho-p44/42 MAPK (Erk1/2) (Thr202/Tyr204) (D13.14.4E) (rabbit, 1:150, Cell Signaling, 4370). Furthermore, the PerkinElmer Opal 4-Color Manual IHC Kit (PerkinElmer, NEL810001KT) was used for the tyramide signal amplification according to the manufacturer's protocol. For introduction of the secondary-HRP the Envision+ /HRP goat anti-Rabbit (Dako Envision+ Single Reagents, HRP, Rabbit, Code K4003) was used. P-Akt and p-Erk were detected using the OPAL 520 and OPAL 690 reagent, respectively.

Immunofluorescence on frozen sections

Tissue samples were dissected and fixed for 20min in 4% paraformaldehyde at RT. Samples were washed in PBS and incubated overnight in 30% sucrose in PBS at 4°C. Tissue samples were then embedded in Tissue-Tek® O.C.T.™ Compound (Sakura 4583) and stored at -80°C. Sections of 10 µm were cut using the Thermo Scientific CryoStar NX70 Cryostat. Sections were stored short term at -20°C. For immunofluorescence, tissue sections were thawed and fixed for 10min in 4% paraformaldehyde on ice. Sections were washed in PBS for 5min at RT, permeabilized in 1% Triton™ X-100 in PBS for 5min at RT and washed in 0.1% Tween®20 (VWR chemicals) in TBS. Sections were incubated in blocking buffer (1%BSA, 10% donkey serum, 0.1% Tween in TBS) for 1h at RT. Subsequently, primary antibodies were incubated overnight at 4°C in antibody diluent (1%BSA, 0.1% Tween in TBS). Sections were washed three times using 0.1% Tween®20 (VWR chemicals, Amresco, 0777) in TBS for 5min at RT and incubated with corresponding secondary antibodies diluted 1:400 in antibody diluent for 1h at RT. Sections were washed three times for 5min at RT, nuclei were stained with DAPI solution (0.5mg/ml) diluted 1:1000 in PBS for 10min and mounted in VECTASHIELD® Antifade Mounting Medium for fluorescence (VECTOR). The following primary antibodies were used: anti-E-Cadherin (rabbit, 1:400, abcam, ab15148), anti-Ki67 (rabbit, 1:200, RM-9106-S0, ThermoFisher), anti-gp100 (rabbit, 1:400, abcam, ab137078), anti-Mitf (rabbit, 1:500, HPA003259, Sigma). The following secondary antibodies were used: donkey-anti-rabbit IgG (H+L) conjugated to Alexa Fluor® 647 or Alexa Fluor® 568 (A31573/A10042, Life Technologies).

Microscope image acquisition

Images were acquired on the Zeiss Axio Scan.Z1 using x20 and x40 objectives and Zeiss ZEN 2 software (Figures 1B, middle and right panel, 1C, 1F, 1H, 2D, middle and right panel, 3B–D, 3F, 4A–4C, right panel, 4D, 4E, 6A–6C, S2A, S2B, S3B, S4A–S4C, S5A, and S5B) or Leica Leitz DMRB Fluorescence Microscope (Figure 7E). All images acquired with the Zeiss Axio Scan.Z1 were automatically stitched during image acquisition using the Zeiss ZEN 2 software. Confocal images were acquired at RT using a Leica TCS SP5 II confocal (Figure 2B) or Nikon A1R Eclipse Ti confocal (Figures 1B, left panel, 2D, left panel, and 4C, left and middle panel). Optical sections of 2,048 × 2,048 pixels were collected.

Live in vivo Imaging

4-HT tail treated Tyr::CreERT2, BRafCA+, Ptenfl/fl, R26RLSL-tdTomato mice were anesthetized using Isoflurane from a precision vaporizer (3,5% for induction; 1,5% for maintenance in oxygen and air). While imaging, mice were placed on a warming pad and the tail was immobilized using a silicon mount and 3% of agarose (Sigma). Murine tail skin was imaged using a HCX IRAPO L25x/0.95 water objective mounted on a SP8 upright microscope (Leica Microsystems) equipped with a Titanium:Sapphire laser (Vision II, Coherent Inc.) tuned at 1050 nm. Optical sections of 1024 × 1024 pixels were collected and image stacks with a z axis interval of 1µm were acquired using two non-descanned Hybrid detectors (RLD HyD, Leica Microsystems) with bandpass emission filters (ET525/50 and ET610/75 m, Chroma Technology). Images were processed using the open-source software ImageJ/Fiji and are viewed as maximum intensity Z-projection. For the stitching of the optical sections the ImageJ/Fiji plugin "3D Stitching" from Preibisch et al. (2009) was used.

Preparation of single cell suspensions

The tail skin or tail epidermis of 4-HT treated Tyr::CreERT2, R26RLSL-tdTomato, or Tyr::CreERT2, BRafCA+, Ptenfl/fl, R26RLSL-tdTomato mice was cut into small pieces and enzymatically digested in 5mg/mL collagenase type I (Sigma) and 5mg/mL collagenase type IV (Sigma) for 20min at 37°C in the dark. The digestion was stopped by adding washing buffer (20% FCS in 1xHBBS) and the digest was pelleted at 1100 rpm for 5 min. After a subsequent washing step in PBS, the digest was incubated in 0,25% trypsin (Thermo Fisher Scientific) for 5min at 37°C in the dark. The reaction was stopped by adding washing buffer and the resulting suspension was centrifuged at 1100 rpm for 5 min. The pellet was resuspended in PBS, passed through a 70 µm cell strainer (Thermo Fisher Scientific) and again centrifuged at 1100 rpm for 5 min. The cell pellet was then resuspended in FACS sorting buffer (5%FCS, 2mM EDTA in F12) and passed through a 45 µm cell strainer (BD Biosciences).

Flow cytometry

For subsequent single cell RNA-Seq analysis, single tdTomato+ cells were sorted into individual wells of a 96 well plate using a BD FACS Aria III (100µm nozzle, 20psi, on the single cell precision mode) containing 2µl of lysis buffer (0.2% Triton X-100, 4units of RNase inhibitor). For subsequent recombination PCR, tdTomato+ cells were sorted into an Eppendorf Tube® using a BD FACS Aria III (100µm nozzle, 20psi, on the purity precision mode) containing 50 µl of buffer ALT (QIAGEN). Cells were gated on tdTomato positivity as well as forward and side scatter (FSC-A versus SSC-A), with additional gates to exclude doublets (FSC-W versus FSC-H and

SSC-W. versus SSC-H) along with a gate excluding dead cells (SYTOX® Blue Dead Cell Stain, Thermo Fisher Scientific, 1 μ M). A 375nm, 10mW laser with a 450/40 BP (bandpass filter) was used to detect SYTOX® Blue.

Recombination PCR

Tyr::CreER^{T2/+}; Braf^{CA/+}; Pten^{fl/fl}; ROSA26R^{LSL-tdTomato/+} mice aged 10-12 weeks were treated with 4-HT on their back skin. 5 days after treatment mice were either shaved or epilated as described earlier and their skin was subjected to single cell preparations. Epilating the back skin at this respective time point after treatment allows to remove all differentiated melanocytes of the hair matrix and allows to isolate remaining bulge melanocytes via FACS based on tdTomato positivity. Shaving the back skin leaves all melanocytes within the hair follicles untouched and subsequent FACS allows to isolate both melanocyte compartments of the hair follicle. Cells were sorted into buffer ALT (QIAGEN) and DNA was extracted using the QIAamp DNA Micro Kit (QIAGEN) according to the manufacturer's protocol. Obtained DNA was then used for PCR analysis with primer pairs for BrafCA (forward primer: 5'-TGAG TATTTTTGTGGCAACTGC-3'; and reverse primer: 5'-CTCTGCTGGGAAAGCGGC-3') and Pten (forward primer: 5'-ACTCAAGG CAGG-GATGAGC-3', and two reverse primers: 5'-AATCTAGGGCCTCTTGTC CC-3' and 5'-GCTTGATATCGAATTCCTGCAGC-3') according to [Dankort et al. \(2007\)](#) and [Lesche et al. \(2002\)](#) respectively.

Single Cell RNA-Seq and data analysis

Full-length RNA-seq from single cells using Smart-seq2 was adapted from ([Picelli et al., 2014](#)). Briefly, reverse transcription was carried out using 25 μ M of TSO. Next, cDNAs were amplified with 25 cycles. Prior quality check with the Bioanalyzer, amplified cDNAs were purified using ampure XP beads (0.8:1 ratio). Sequencing libraries were generated using 1/4th of recommended volumes of the Nextera XT kit (Illumina). The input cDNA was diluted 1:4 and the tagmentation reaction was performed for 9min. Amplification of adaptor-ligated fragments was performed using Nextera XT indexing primers (kit V2 set A-D, Illumina). 96 individually indexed libraries were pooled and cleaned up together using ampure XP beads (0.6:1 ratio) before Bioanalyzer quality check. Individual pools were pooled in equimolar amounts before sequencing on the Nextseq500 (Illumina) instrument using 75bp single-end reads. Following sequencing on the NextSeq500, BAM files were converted to merged, demultiplexed FASTQs and cleaned using FastQC (0.11.4). Reads were then mapped to the mouse genome (mm10_GRCm38) using STAR (2.4.1b-foss-2014a). Cells with less than 100,000 reads and/or 1000 genes expressed were discarded. Furthermore, only cells with an average expression level > 3 of a curated list of housekeeping genes (n = 84) were kept ([Tirosh et al., 2016](#)). Taking into account these cut-offs, 144 of 215 sequenced single cells were qualified for further analyses (GEO: GSE100607 <https://www.ncbi.nlm.nih.gov/geo/query/acc.cgi?acc=GSE100607>; Reviewers token: krmdequqvztkxcj). Highly variable genes (HVGs) were identified following the Kharchenko workflow ([Kharchenko et al., 2014](#)): library size factor normalization (DESeq) and winsorization of the data prior plotting variation (logCV2) over mean expression (logmeans). After fitting a regression line to the data, genes were ranked and selected by their significance of deviation from the fit (adjusted p value < 1e-3, n = 1268 HVGs). Based on the expression of 1268 HVGs, 144 single cells were clustered in an unsupervised manner using non-negative matrix factorization as dimension reduction approach (run = 40, rank = 10, in MeV 4.8.1). Single-cell differential expression analysis (SCDE) was performed between the different NMF-clusters using the total gene expression matrix (144 cells x 14962 genes) ([Kharchenko et al., 2014](#)). SCDE analysis generated a Z-score ranked gene list for each NMF cluster of which the top 100 candidates were subjected to Ingenuity Pathway Analysis (IPA). Characteristic gene signatures per NMF cluster (comprising 20-30 genes each) were generated based on functional enrichment and highly ranked genes. To measure the activity of an entire gene expression signature per cell we used the AUCell algorithm ([Aibar et al., 2017](#)). We clustered the 144 single cells using t-distributed stochastic neighbor embedding (t-SNE, perplexity = 10, initial_dims = 20, max_iter = 1000) based on all genes giving rise to the 3 functional SCDE-IPA signatures and colored coded the cells according to their AUCell score (signature-activity). Transcriptional network analysis was performed on the top 50 ranked SCDE genes per NMF cluster using iRegulon (Version 1.2 as cytoscape plugin). Gene set enrichment analysis (GSEA version 2.2.1) was performed by ranking SCDE genes based on their cZ-score as metric (cluster 1 and 2 of mouse single-cell RNaseq data). Human gene signatures were obtained from a proliferative and invasive melanoma gene set ([Verfaillie et al., 2015](#)).

QUANTIFICATION AND STATISTICAL ANALYSIS

For mouse experiments, n represents the number of independent biological replicates. All groups consisted of age-matched mice. Experiments were not blinded. Details with respect to the experimental design and the statistical analysis are provided in the Detailed Methods section or below.

Quantification of melanocyte number

A total of 30 tail units of at least 3 iDct-GFP mice per time point or a total of 10 tail units of at least 3 *Tyr::CreER^{T2/+}; ROSA26R^{LSL-tdTomato/+}* mice were analyzed. To determine the absolute melanocyte number for each time point respectively, epidermal whole mounts were stained for gp100 and imaged using the Axio Scan.Z1 and ZEN 2 software. Expression of H2BGFP/tdTomato or co-expression of H2BGFP/tdTomato and gp100 was analyzed. Cells were either scored as H2BGFP+/tdTomato+gp100+ or H2BGFP+/tdTomato+gp100- and counted with regard to their location within one tail unit (scale versus inter-scale). Melanocyte numbers were averaged for each individual mouse and individual time point. Values were then normalized and are depicted as percentage.

Quantification of clone size

A total of 3-5 tail units from 3 *Tyr::CreER^{T2/+}; BRaf^{CA/+}; Pten^{fl/fl}; ROSA26R^{LSL-confetti/LSL-confetti}* mice per time point were analyzed. To determine the number of cells per clone, epidermal whole mounts were imaged using the Axio Scan.Z1 and ZEN 2 software. For each tail unit all cells of a unique color in close proximity were scored as a group of cells and the size (= cell number) of the different cell groups were counted. If no cells were in close proximity the group size was scored as 1. We then defined the minimal size of a group of cells to be considered as a clone. The clone size at each time point was defined as the upper 80%-range of the size of all cell groups. With a maximal group size of 3, 8, and 16 for days 7, 14, and 21, respectively this resulted in a clone size of at least 2, 3, and 4 cells per group for days 7, 14, and 21 respectively. At least 3 tail units were analyzed to score the average number of clones per tail unit using the different clone sizes per time point. For determining the average clone size, the size of each clone considered in the analysis of the clone number was used.

DATA AND SOFTWARE AVAILABILITY

The accession number for the single-cell RNA-sequencing data reported in this paper is GEO: GSE100607. A detailed description of the data analyses can be found in the [Methods Details](#) and the [Quantification and Statistical Analysis](#) section. A list of the software that was used for the respective analyses can be found in the [Key Resources Table](#).